

Received 30 July 2022, accepted 12 August 2022, date of publication 19 August 2022, date of current version 8 September 2022.

Digital Object Identifier 10.1109/ACCESS.2022.3200335

RESEARCH ARTICLE

Design, Modeling, and Analysis of a 3-D Spiral Inductor With Magnetic Thin-Films for PwrSoC/PwrSiP DC-DC Converters

CHANDRA SHETTY¹, (Member, IEEE), AND DANIEL C. SMALLWOOD¹

Micro and Nano Systems Centre, Tyndall National Institute, University College Cork, Cork 21, T12 R5CP Ireland

Corresponding author: Chandra Shetty (chandra.shetty@tyndall.ie)

This research was supported by Tyndall National Institute, University College Cork and Science Foundation Ireland under the ADEPT Project No. 15/IA/3180 “Advanced Integrated Power Magnetism Technology—From Atoms to Systems”.

ABSTRACT A solution architecture for monolithic system-on-chip (SoC) power conversion is in high demand to enable modern electronics with a reduced footprint and increased functionality. A promising solution is to reduce the microinductor size by using novel magnetically-enhanced 3-D design topologies. This work presents the design, modeling, and analysis of a 3-D spiral inductor with magnetic thin-films for power supply applications in the frequency range of 3-30 MHz. A closed-form analytical expression is derived for the inductance, including both the air- and magnetic-core contributions. To validate the air-core inductance model, we implement a 3-D spiral inductor on PCB. The theoretical calculation of air-core inductance is in good agreement with experimental data. To validate the inductance model of the magnetic-core, a 3-D spiral inductor is modeled with Ansys Maxwell electromagnetic field simulation software. A winding AC resistance model is additionally presented. We perform a design space exploration (DSE) to investigate the significance of the 3-D spiral inductor structure. Two important performance parameters are discussed: dc quality factor (Q_{dc}) and ac quality factor (Q_{ac}). Also, a 3-D spiral inductor structure with magnetic thin-films is characterized in Ansys Maxwell to estimate its potential, and a novel fabrication method is proposed to implement this inductor. The measured relative permeability (μ_r) and the magnetic loss tangent ($\tan \delta$) of Co-Zr-Ta-B magnetic thin-films, developed in-house, are used to simulate the proposed structure. The promising results of the DSE can be easily extended to improve the performance of other 3-D inductor topologies, such as the solenoid and the toroid. The numerical simulations reveal that the 3-D spiral inductor with magnetic thin-films has the potential to demonstrate a figure-of-merit (FOM) that is significantly higher than traditional inductors.

INDEX TERMS Power supply on chip (PwrSoC), power supply in package (PwrSiP), 3-D spiral inductor, partial inductance, dc quality factor (Q_{dc}).

I. INTRODUCTION

Modern electronic devices demand increased functionality coupled with device miniaturization. This highlights the challenge of power delivery to these highly integrated devices, where traditional approaches to point-of-load power conversion (the converter is placed in proximity to the load

The associate editor coordinating the review of this manuscript and approving it for publication was Valentine Novosad.

to provide a precise voltage) can no longer be applied. In the case of point-of-load power conversion [1], [2], each switching regulator requires discrete passive components (i.e., inductor and capacitor). Specifically, the inductor is the pain point due to its large footprint and height profile. The ideal solution here is to have the power conversion circuitry integrated directly with the load (e.g., CPU, SOC); that is, the load and power supply are monolithically integrated. In other words, we need to realize a system-on-chip (SoC) [see Fig. 1]

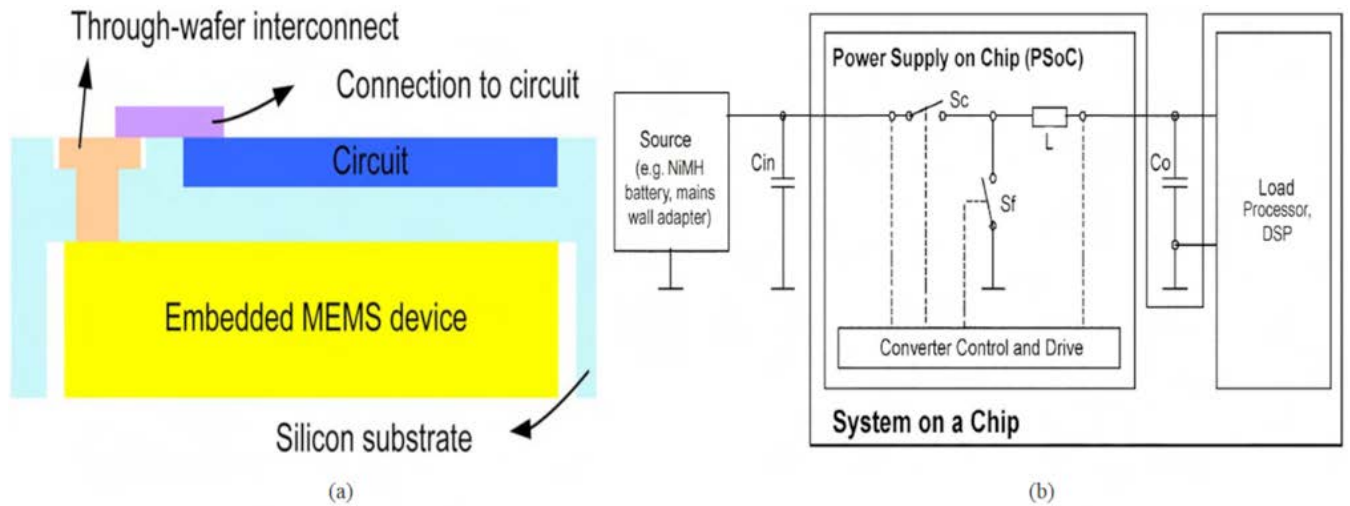


FIGURE 1. (a) Conceptual approach for the realization of power supply on chip (PwrSoC) [3] (© 2013 IEEE) and (b) concept of system-on-chip (SoC): load and power supply are incorporated within the same monolithic unit [4] (© 2005 IEEE).

solution. Furthermore, the holy-grail in power management is to make the multiple passives “disappear” onto or into the SOC substrate/package.

A. BACKGROUND AND MOTIVATION

A key roadblock in the realization of Power Supply on Chip (PwrSoC)/ Power Supply in Package (PwrSiP) solution is the integration of bulky magnetic passive components (i.e. inductors and transformers) [5], [6]. The terms PwrSiP and PwrSoC are defined as follows [7], [8]:

- 1) **PwrSiP**: Separate chips (switches drivers, controller) within the same package with external inductor/passives. The passives (inductor and capacitor) and the PMIC can be either assembled side by side or stacked on each other.
- 2) **PwrSoC**: A single chip (containing switches, drivers, and controller) with integrated inductor/passives. Here the inductor/passives will be integrated onto the power management IC (PMIC), i.e., monolithic integration.

As the size of the magnetic passive components shrinks, integration becomes easy [see Fig. 2]. The size of the magnetic components can be reduced either by (a) increasing the frequency, or (b) employing advanced magnetic passive components (AMPC), which exhibits high power density. Although the former approach results in improved load transient response in the case of DC-DC converters (depending on bandwidth [9]), it has shortcomings such as switching loss, magnetic-core loss, substrate loss and electromagnetic interference (EMI). Consequently, the latter approach is the preferred choice. However, the research on AMPC is still in its infancy and requires considerable progress to make the application of AMPC practicable.

B. REVIEW OF PREVIOUS WORK

Recently, there has been a great interest in developing 3-D inductors as this structure has the advantage of high

inductance density over a conventional 2-D inductor [11], [12]. The structural difference between 2-D and 3-D inductors is illustrated in Fig. 3. Three-dimensional (3-D) inductors can be classified as in-substrate (also referred to as in-chip or in-silicon) inductors and on-substrate (also referred to as on-chip or on-silicon) inductors. Although in-silicon inductors are challenging to fabricate, this type of inductor makes use of unused substrate volume, resulting in a low profile inductor, and hence, improved volumetric inductance density. As the inductor footprint reduces, the DC ratio of inductance to resistance (L_{dc}/R_{dc}), also known as the DC quality factor (Q_{dc}) [13], [14], decreases significantly [15]. Inductors employed in PwrSiP [16], [17] and PwrSoC [4], [17] carry current which is composed of AC (ripple current) and DC components. DC resistance (DCR) is a major contributor to copper loss due to a large DC component in the inductor current, which indicates that there is a necessity to design inductors that exhibit lower DCR (R_{dc}) and in turn higher Q_{dc} .

As discussed in [19], the DCR of 3-D toroidal inductors can be reduced by the following ways: (a) connecting vertical conductors in parallel [see Fig. 4] and (b) increasing the winding cross-section. However, the traditional 3-D inductor structure such as a toroid allows a limited number of parallel connections and a small increase in the winding cross-section due to the footprint constraint. As a result, the improvement in DCR is not satisfactory. Also, the parallel connection of vertical conductors requires a trapezoidal-shaped bottom and top radial conductors [see Fig. 4(b)]. A trapezoidal-shaped conductor does not have a closed-form analytical solution for the inductance, which makes it challenging to design the inductor. The characterization of non-standard structures such as trapezoidal-shaped conductors in finite element analysis (FEA) takes a significant amount of time and memory. Another disadvantage of parallel connection is the increase of parasitic capacitance.

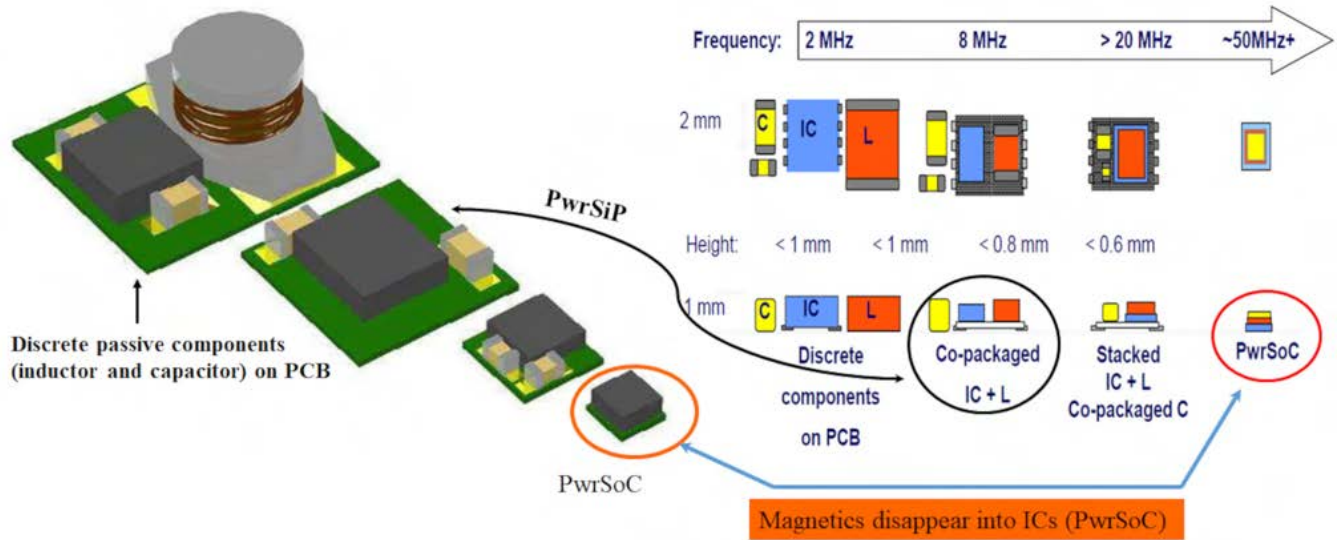


FIGURE 2. Evolution PwrSiP to PwrSoC [10] (© 2010 IEEE), [1] (© 2012 IEEE).

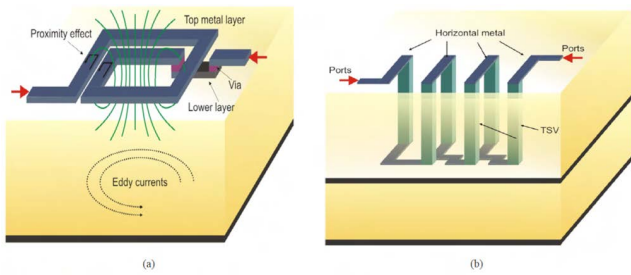


FIGURE 3. Physical structure of micro inductors: (a) 2-D inductor and (b) 3-D inductor [18] (© 2011 IEEE).

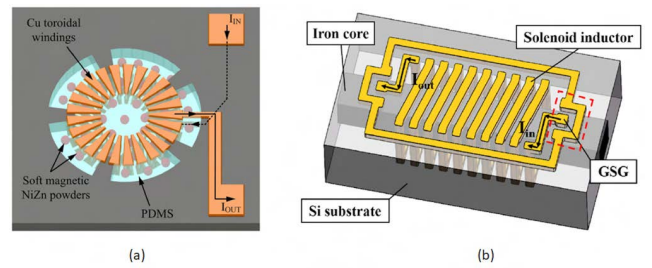


FIGURE 5. Three dimensional (3-D) inductors with magnetic-core: (a) toroid [5] (© 2018 IEEE) and (b) solenoid [27] (<https://creativecommons.org/licenses/by/4.0/>).

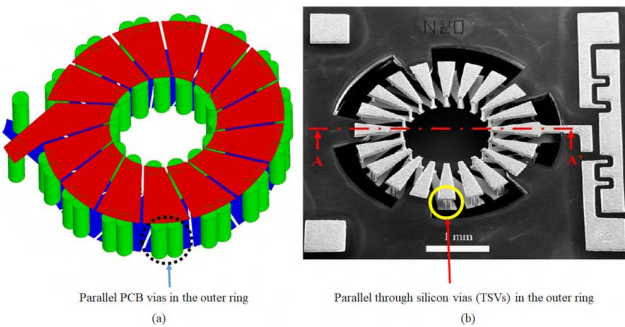


FIGURE 4. Outer ring vertical conductors are connected in parallel to reduce DCR: (a) PCB inductor [20] (© 2017 IEEE) (b) silicon inductor [19] (© 2018 IEEE).

Alternatively, Q_{dc} can be improved either by (a) decreasing negative mutual inductance, or (b) increasing positive mutual inductance; the former can be achieved by increasing the distance between conductors with opposite directions of current flow and the latter is accomplished by placing conductors with the same direction of current flow closer. The drawbacks are that (a) in the first approach, the footprint will

increase, and (b) the second approach increases the interwinding capacitance.

In [15], [21], and [22], the study has been carried out to optimize the Q_{dc} of on-chip inductors. These are magnetic-core inductors. The Q_{dc} of magnetic-core inductors is better than air-core inductors due to enhanced inductance contributed by the magnetic-core. However, the integration of a magnetic-core has following disadvantages: (a) it involves core loss [23] (b) it is challenging to integrate the core [24], [25], and (c) it is difficult to introduce anisotropy into the core [26], [14]. In the previous research on 3-D inductors [5], [27] [see Fig. 5], a magnetic-core is integrated to improve the inductance density. However, these inductors are not suitable to operate at high-frequency (HF) (3-30 MHz) as the core is solid (non-laminated); they suffer from low Q_{ac} ($2\pi fL_{ac}/R_{ac}$) at HF due to large eddy currents. In [24], even though the laminated core is embedded, the inductor occupies a large footprint. This implies the necessity of a 3-D spiral inductor structure where it is relatively easy to integrate a thin core and induce anisotropy while maintaining high Q_{ac} and Q_{dc} .

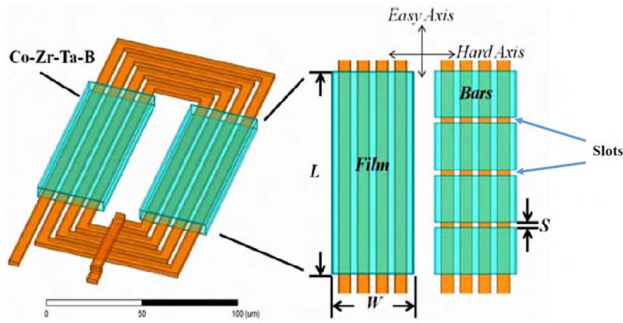


FIGURE 6. Slotting, which introduces slots in the continuous magnetic film in the direction perpendicular to the inductor wire with an intention to cut off eddy current flow and hence reduce loss in the magnetic film [28] (© 2013 IEEE).

Traditionally, the effect of eddy currents in the magnetic-core can be suppressed by employing (a) multiple laminations (b) sub-micron film thicknesses, (c) slotting (magnetic films are patterned into bars, see Fig. 6) [28], and (d) high resistivity magnetic material. The first approach leads to increased cost as well as process complexity [29]. Also, it involves displacement eddy current loss [30]. The second approach degrades the power handling capacity of the film [26]. Finally, the third approach is not suitable for power supply frequency range, which is typically 1-100 MHz, as it suffers from low quality factor [28]. In this work, single-layer magnetic thin-films of high resistivity are distributed along the radial direction. The advantages of employing single-layer magnetic thin-films are the elimination of displacement eddy current loss and lamination cost.

Another factor that degrades the Q_{ac} of 3-D inductors is substrate loss. Several methods are proposed to reduce the substrate loss: (a) introduction of a microchannel [12] [see Fig. 7(a)], (b) employing a high resistivity substrate [31], and (c) removing the silicon core partially or completely [19] [see Fig. 7(b)]. Other methods are discussed in [32].

In this paper, we report a novel 3-D spiral inductor with thin-films for PwrSoC/PwrSiP dc-dc converters in the frequency range of 3–30 MHz. The specific contributions of this paper include: to the best of our knowledge, we herein introduce for the first time, the concept of a three-quarter turn in the context of 3-D microinductor design, which is a fundamental unit cell that can be used to construct novel 3-D inductor topologies and thereby expand the bounds of the DSE. Moreover, as presented in section II, we demonstrate that a three-quarter turn exhibits a better Q_{dc} than a full turn, 2) a simple closed turn approach is adapted to derive an analytical solution for the air-core inductance of the proposed 3-D inductor. This simple approach can be extended to 2-D spiral air-core inductors, for which relatively complicated methods have previously been reported for inductance models [37]. The air-core 3-D spiral inductor is implemented in a PCB and electrically characterized to validate the inductance model. Also, a winding AC resistance model is presented. In addition, analytical equations are presented for the

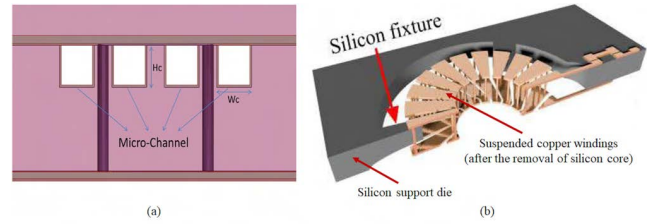


FIGURE 7. Substrate loss reduction in 3-D TSV inductors by means of (a) microchannel shields [12] (© 2015 IEEE) (b) a complete removal of silicon core [19] (© 2018 IEEE).

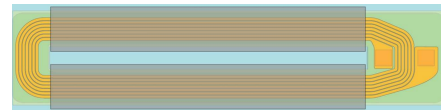


FIGURE 8. Topology of the 2-D racetrack inductor with thin-films [33] (<https://creativecommons.org/licenses/by/4.0/>).

resistance and inductance of three-quarter and full turns with circular and rectangular cross sections, 3) a novel fabrication method is proposed for a magnetically-enhanced 3-D spiral microinductor with radially oriented magnetic materials in a unique quadrant topology, 4) we discuss the advantages of using single-layer thin-films and a high resistivity substrate, as well as the significance of working in the frequency range of 3-30 MHz and the potential impact of EMI in the given frequency range. Furthermore, Table 1 summarizes the benefits of a 3-D spiral inductor with thin-films as compared to a 2-D spiral inductor with thin-films.

C. SCOPE OF THIS WORK

In this work, the traditional spiral inductor structures such as the planar and the two-layer are modified to improve Q_{dc} and Q_{ac} . The goal is to maximize volume coverage, that is, increase the dimensions of the winding conductors to lower the DCR. Also, the distance between the opposite current carrying vertical conductors is increased to reduce the number of conductors, which in turn reduces DCR without significantly affecting the air-core energy storage density of the inductor. The winding conductors are arranged so that the direction of currents in all the windings are the same, which contributes to positive mutual inductance. Also, this strategic arrangement of conductors reduces substrate loss as most of the magnetic field lines due to vertical conductors cancel each other inside the substrate except the strong H -fields near the vertical conductors, details are discussed in section III. Another important reason for the reduction in the substrate loss is the magnetic field direction of vertical conductors is parallel to the substrate plane. Thin-film magnetic-cores with a thickness less than the skin depth are integrated to improve the inductance density. Unlike 3-D solenoidal and toroidal inductors (winding surrounds the core), the role of conductor and core is switched in 3-D spiral inductor structures with magnetic thin-films (core surrounds the winding) to optimize the performance. This novel approach offers a low reluctance

TABLE 1. List of advantages of 3-D spiral inductor with thin-films over 2-D inductor with thin-films.

Parameter	3-D Spiral inductor with thin-films*	2-D inductor with thin-films*
Topology	✓ Comprised of standard conductor geometries such as circular and rectangular, which helps with design, simulation and developing closed loop solutions for inductance and resistance. A spiral topology eliminates parasitic capacitance between the top and bottom conductors of the same turn. Also, the capacitance between turns can be much smaller than in a 2-D spiral inductor. This topology is constructed from three quarter turns which exhibit better Q_{dc} than full turns, which are used for constructing 2-D topologies, as discussed in section II.	✗ This structure often employs complicated geometries, such as racetrack shaped copper windings (as illustrated in Fig. 8), which are difficult to design.
Inductance density	✓ This structure makes use of unused substrate volume, and as a result, it exhibits a high inductance density. Moreover, we can fine-tune the inductance density by varying the vertical conductor cross section (magnetic-core conductors). The basic idea is to control the reluctance path, whereby smaller (larger) cross section vertical conductors exhibit a low (high) reluctance path and a high (reduced) inductance density.	✗ Since this structure has a planar topology, it requires more substrate area than its 3-D counterpart to enable the same inductance density. The inductance density can be improved by reducing the conductor cross section, but this will increase the already relatively higher DCR as compared to the 3-D structure, which is due to the herein discussed L_{dc}/R_{dc} ratio parameter.
L_{dc}/R_{dc} ratio	✓ It is possible to fine-tune the DCR of 3-D spiral inductors by constructing vertical conductors with different cross sections on the same substrate. The magnetic-core conductor cross section (pillars or vertical conductors) can be varied depending on the required inductance while holding the air-core conductor cross section (interconnects) constant. The impact of magnetic-core conductors cross section on L_{dc} , R_{dc} , and Q_{dc} is illustrated in Fig. 9**.	✗ Even though the conventional 2-D spiral inductor structure is easier to fabricate when compared to its 3-D counterpart, it would be very difficult to fabricate air-core and magnetic-core conductors with different cross sections in a 2-D topology. In the literature, there are no reports of a 2-D spiral inductor with a non-uniform conductor cross section. On the other hand, 3-D inductors have been reported that comprise conductors with different cross sections. For example, [20] features a fabricated 3-D inductor that comprises pillars/vertical conductors with a circular cross section and radial conductors/interconnects with a trapezoidal shape.
Q-factor	✓ Magnetic (air) core conductors produce an in-plane (out-of-plane) magnetic field. An in-plane magnetic field generates eddy currents perpendicular to the substrate. Since less flux penetrates the substrate, substantially lower eddy currents are induced. This increases the quality factor of the 3-D inductor. The in-plane magnetic field in a 3-D inductor is illustrated in Fig. 10.	✗ As 2-D spiral inductors are comprised of only planar conductors, the magnetic field is always out-of-plane. Out-of-plane magnetic fields induce eddy currents parallel to the substrate, which significantly impacts substrate loss and severely degrades the inductor Q-factor. The out-of-plane magnetic field in a 2-D inductor is illustrated in Fig. 11.
Saturation current	✓ The saturation current can easily be tuned by controlling the flux density. Since the flux density in the core is dependent on the cross section of the magnetic-core conductor(s), the saturation current can be modulated without influencing the air-core conductor inductance and resistance.	✗ It is not possible to easily control the saturation current, as the inductor is designed such that the air and magnetic-core conductors have a uniform cross section. The reason for this is herein explained while dealing with the L_{dc}/R_{dc} parameter.

* To simplify the comparison, we have arranged the inductors into two groups comprising air and magnetic-core conductors.

** While varying the radius of the magnetic-core conductors, all other design parameters such as footprint, interconnect cross-section, core thickness, etc. are kept constant. The specifications considered for this study are given in Table 2.

path for the flux, resulting in high inductance density. The thin-film magnetic-cores are arranged so that flux travels along the hard axis of the core, which is essential for high-frequency operation [26], and the eddy currents flow in the axial direction, in the direction opposite to the current in the vertical conductors of the winding. More details on the 3-D spiral inductor with magnetic thin-films are given in section III.

Even though the 3-D spiral inductor with thin-films shares common features with 2-D inductors with thin-films, there are significant differences between these two structures, both morphologically and functionally, as illustrated in Table 1.

In this paper, we propose a reduced frequency of operation (3-30 MHz) to mitigate the problems such as switching loss, magnetic-core loss, substrate loss, and electromagnetic interference (EMI). The central idea of a reduced frequency of operation approach to improve the FOM of proposed inductor can be justified as follows. It is well known that increasing the frequency will reduce the inductance requirement for switching converters [35], [36], [37], [38]. However, one cannot increase the switching frequency extremely high for the reasons mentioned earlier. The 3-D spiral inductor with magnetic thin-films exhibits the required inductance to operate a

switching converter circuit at the proposed frequency of operation. We have demonstrated this by taking a buck converter that operates in continuous conduction mode (CCM) as an example. The example converter has the following specifications: input voltage (V_{in}) = 3 V, output voltage (V_o) = 1 V, frequency (f) = 30 MHz, duty cycle (D) = 0.33, load current (I_o) = 1 A, and load resistance (R) = 1 Ω . The minimum inductance (L_{min}), estimated with the help of (1) [39], required for the continuous conduction mode is 11.16 nH. This estimated value is much less than the inductance of the proposed inductor [see Table 4], which means that the example converter can operate in CCM if the proposed inductor is employed for energy storage. Larger inductance results in lower ripple and hence reduction in RMS value of inductance current, which leads to higher efficiency. In other words, the 3-D spiral inductor with magnetic thin-films can serve as an energy storage element for dc-dc converters while maintaining high FOM.

$$L_{min} = \frac{(1 - D)R}{2f} \quad (1)$$

A limitation of the 3-D spiral inductor structure is that the fluxes are not confined, which leads to magnetic interference

(radiated EMI) with other circuits. If the stray fields (external magnetic field) that it produces can be mitigated, it could be a promising candidate for integrated power supply applications. A brief introduction to the concept of EMI and mitigation methods is provided below.

There are two types of EMI: conducted and radiated. Radiated EMI is a concern only above 30 MHz [40], [41], [42], [43]. At very high frequency (>30MHz), conductors can become antennas and radiate RF energy and potentially generate harmful EMI. The radiated EMI can be mitigated by a shielding technique. As far as conducted EMI is concerned, the noise in the frequency range of 3-30 MHz can be reduced by EMI filtering [40]. For example, the input current in a buck converter is rich in harmonics [41]. An EMI filter can be employed to attenuate the switching harmonics present in the converter input current [44]. The maximum frequency that we propose in this paper is 30 MHz. As a result, the 3-D inductor with thin-films can be employed in switching converters without imposing potential harmful effects of radiated EMI.

The paper is organized as follows: after the introduction, we study the Q_{dc} of different 3-D inductor winding components in section II. The 3-D spiral inductor with magnetic thin-films is presented in section III. Section IV discusses the integration of magnetic thin-films in a 3-D spiral inductor structure and fabrication method. In section V, the accuracy of analytical models for the inductances of the winding and the magnetic thin-films are discussed, and also the FOM of 3-D spiral inductor with magnetic thin-films is compared with previously published work. Finally, the paper is concluded in section VI.

II. DESIGN SPACE EXPLORATION

The process of investigating optimal parameter combinations, which results in the highest inductor performance, can be termed as design space exploration (DSE). In this work, a design space is created graphically to determine the impact of design parameters on Q_{dc} .

Three-dimensional (3-D) inductor structures can be formed by connecting a finite number of full turns or three-quarter-turns (0.75-turns) in series. Three-quarter and full turns, which are composed of through-silicon-vias (TSVs) and redistribution layers (RDLs), are shown in Fig. 12. In this paper, we use the term copper pillars (or simply pillars) for TSVs and interconnects for RDLs. The pillar cross-section can be circular, rectangular, or square. Similarly, the interconnect cross-section can be rectangular or square. In this section, we study the Q_{dc} of individual 3-D inductor winding components. Also, we explore the significance of the DC internal inductance of pillars and interconnects. Conclusions from this study are given at the end of this section.

A. DC INTERNAL INDUCTANCE (L_{in})

The internal inductance of a circular pillar ($L_{circ,in}$) [45] and a rectangular pillar ($L_{rect,in}$) [46] are given by (2) and (3),

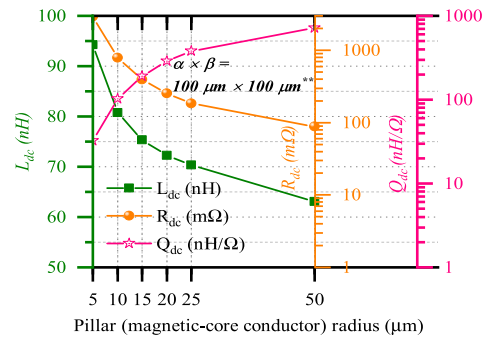


FIGURE 9. Impact of magnetic-core conductor radius on L_{dc} , R_{dc} , and Q_{dc} .

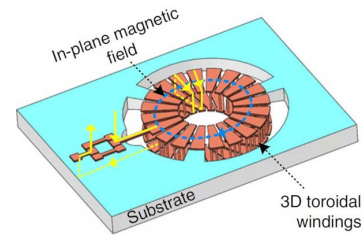


FIGURE 10. In-plane magnetic field in a 3-D inductor [34] (<https://creativecommons.org/licenses/by/4.0/>).

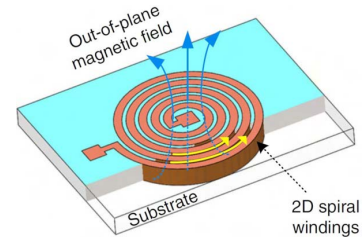


FIGURE 11. Out-of-plane magnetic field in a 2-D inductor [34] (<https://creativecommons.org/licenses/by/4.0/>).

respectively.

$$\begin{aligned}
 L_{circ,in}(l_{cp}) &= \frac{\mu_o l_{cp}}{8\pi} \\
 L_{rect,in}(l_{rp}, \alpha, \beta) &= \frac{\mu_o l_{rp}}{8\pi} \\
 &\times \left(\frac{4.18\alpha^3\beta + 51.90\alpha^2\beta^2 + 4.18\alpha\beta^3}{\alpha^4 + 16.09\alpha^3\beta + 28.2\alpha^2\beta^2 + 16.09\alpha\beta^3 + \beta^4} \right)
 \end{aligned} \tag{3}$$

where l_{cp} is the length of the circular pillar, l_{rp} , α , and β are the length, width, and thickness of the rectangular pillar, respectively and μ_o ($4\pi \times 10^{-7} H/m$) is the permeability of free space.

Fig. 13(a) and (b) show the variation of $L_{circ,in}$ and $L_{rect,in}$ for different dimensions, respectively; simulation and analytical expression results are compared. The lengths of the pillar (i.e., 200 μm , 280 μm , 350 μm , 500 μm) are chosen

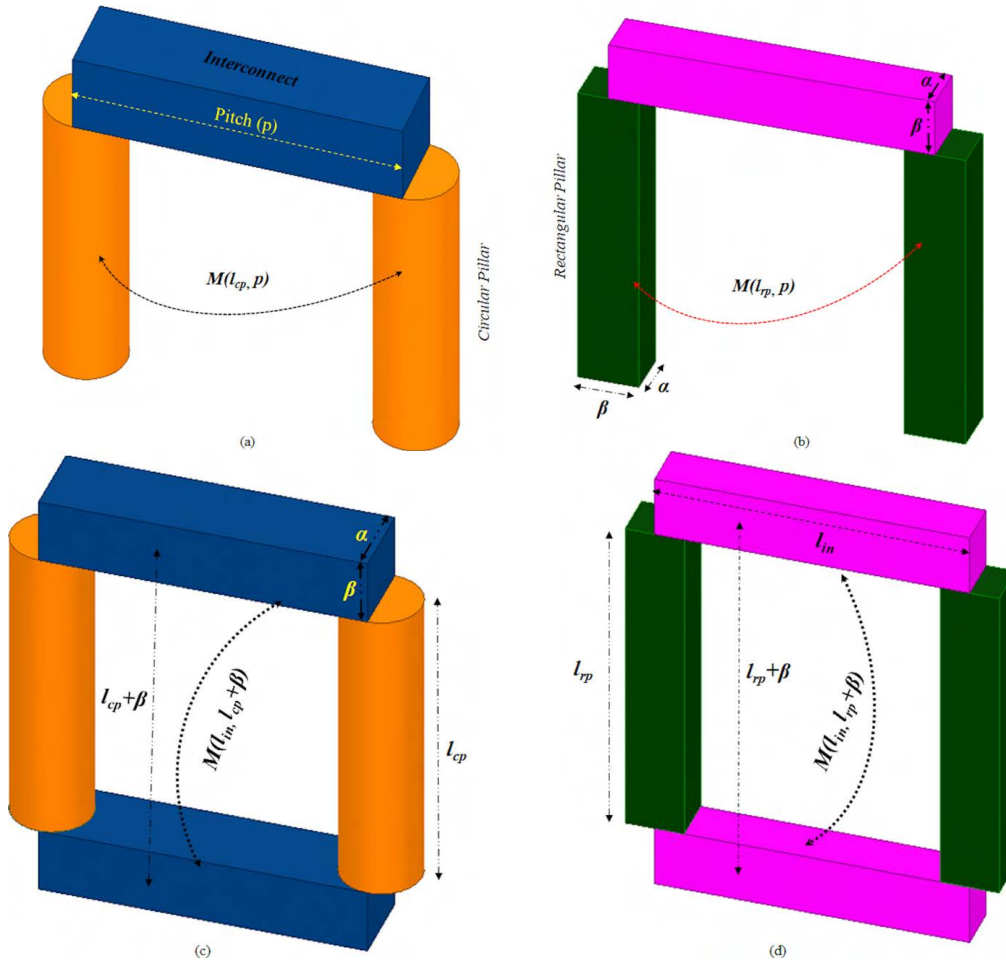


FIGURE 12. Types of turns: (a) Three-quarter-turn (0.75-turn) with circular pillars (b) Three-quarter-turn (0.75-turn) with rectangular pillars (c) Full-turn with circular pillars, and (d) Full-turn with rectangular pillars.

from previous publications [5], [17], [47]. From the graphical study, we see that $L_{rect,in}$ reaches a maximum value when the width (α) becomes equal to the thickness (β). Therefore, we will use square conductors (pillars and interconnects) as a special case of rectangular conductors for further study on the Q_{dc} of different 3-D inductor components.

From Fig. 13, we see that the analytical expression for the internal inductance of a rectangular pillar is more accurate for thin shapes and square pillar geometries, while there is an exact correlation between analytical and FEA results for circular pillars for all dimensions. The reason can be explained as follows. A circular conductor exhibits symmetry that allows the application of Ampere’s law to find the total magnetic flux inside the conductor, and thereby the internal inductance, without the requirement of evaluating any integrals. On the other hand, a rectangular conductor is less symmetrical, which requires complicated numerical integration to compute the internal inductance. Consequently, the closed-loop expression for the internal inductance of a rectangular geometry is less accurate than the circular geometry.

Observation 1: The internal inductance of a circular pillar is independent of the radius. On the other hand, the internal inductance of a rectangular pillar is a maximum when the width (α) is equal to the thickness (β), i.e., a square pillar.

B. Q_{dc} OF A SINGLE PILLAR

Here we study the Q_{dc} of pillars with rectangular and circular cross-sections. Simplified analytical formulas are considered to develop an easy understanding of the relation between Q_{dc} and the conductor dimensions. However, the exact formulas are used for presenting data in graphical form. The exact formulas are given in Appendix I.

1) A SINGLE CIRCULAR PILLAR

Simplified formula for the self-partial inductance (L_{circ}) [48] and resistance (R_{circ}) of circular cross section pillars are given by (4) and (5), respectively, where r is the radius.

$$L_{circ}(l_{cp}, r) = \frac{\mu_0 l_{cp}}{2\pi} \left[\ln \left(\frac{2l_{cp}}{r} \right) - 0.75 \right] \quad (4)$$

$$R_{circ}(l_{cp}, r) = \frac{\rho l_{cp}}{\pi r^2} \quad (5)$$

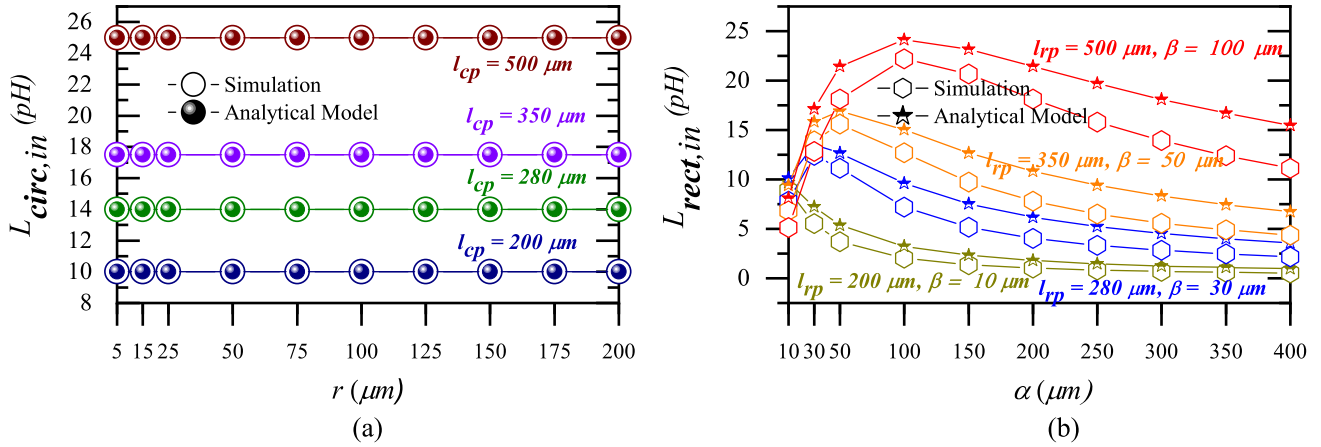


FIGURE 13. Variation of internal inductance of a single-pillar for different dimensions. (a) Circular pillar and (b) Rectangular pillar.

From (4) and (5), we see that there is a trade-off between DCR and self-inductance. The self-inductance of a circular pillar can be improved either by decreasing r or increasing l_{cp} , but this will increase the resistance by the factor of r^2 or l_{cp} . This makes it notoriously difficult to determine the effect of the variation of pillars dimensions on performance. To understand this easily, we have carried out a graphical analysis, as shown in Fig. 14(a), where Q_{dc} is plotted against radius r and length l_{cp} .

2) A SINGLE RECTANGULAR PILLAR

The formulas for the self-partial inductance (L_{rect}) [49] and resistance (R_{rect}) of rectangular interconnects are given by (6) and (7), respectively. The self-inductance of a rectangular conductor can be increased either by decreasing α and β or increasing l_{rp} , but this will increase the resistance by the factor of $\alpha \times \beta$ or l_{rp} . Similar to the previous case, we have carried out a graphical analysis, as shown in Fig. 14(b), where Q_{dc} is plotted against length l_{rp} and width α . We have considered a square cross-section as a special case of a rectangular cross-section for the study for the reason mentioned earlier.

$$L_{rect}(l_{rp}, \alpha, \beta) = \frac{\mu_0 l_{rp}}{2\pi} \left[\ln \left(\frac{2l_{rp}}{\alpha + \beta} \right) - 0.75 \right] \quad (6)$$

$$R_{rect}(l_{rp}, \alpha, \beta) = \frac{\rho l_{rp}}{\alpha\beta} \quad (7)$$

Observation 2: The Q_{dc} of pillars increases with cross section and length. For cross section, the Q_{dc} increases exponentially for both circular and rectangular pillars, and for length from $l_{cp/rp} = 200 \mu\text{m}$ to $l_{cp/rp} = 500 \mu\text{m}$, the increment in Q_{dc} is 31.34-77.30% for circular pillars and 25.48-91.05% for rectangular pillars. The lowest (31.34%) and highest (77.30%) values in the increment range correspond to radii $5 \mu\text{m}$ and $200 \mu\text{m}$, respectively, for circular pillars. Similarly, the lowest (25.48%) and highest (91.05%) values in the increment range are corresponding to $\alpha = \beta = 10 \mu\text{m}$ and $\alpha = \beta = 400 \mu\text{m}$, respectively, for rectangular pillars. Simulated values were used for these and the following percentages.

Observation 3: The Q_{dc} of a rectangular pillar is 27.36-29.15% higher than a circular pillar for approximately the same footprint and length. The comparisons are made at the lowest and highest Q_{dc} values, which occurs at the smallest and largest of pillar volumes, respectively. In this study, the smallest volume corresponds to $r = 5 \mu\text{m}$, $l_{cp} = 200 \mu\text{m}$ and the largest volume corresponds to $r = 200 \mu\text{m}$, $l_{cp} = 500 \mu\text{m}$ for circular conductors. Similarly, the smallest volume corresponds to $\alpha = \beta = 10 \mu\text{m}$, $l_{rp} = 200 \mu\text{m}$ and largest volume corresponds to $\alpha = \beta = 400 \mu\text{m}$, $l_{rp} = 500 \mu\text{m}$ for rectangular conductors.

C. Q_{dc} OF AN INTERCONNECT

Interconnects usually have a rectangular or square cross section. Since we have already studied the Q_{dc} of a square cross section, we can use the same result. The interconnect length is denoted as l_{in} .

D. Q_{dc} OF TWO PARALLEL PILLARS

1) TWO PARALLEL CIRCULAR PILLARS

To estimate the Q_{dc} , we need to compute the inductance as well as the resistance. The inductance of two parallel connected circular pillars, L_{pac} , is half of the sum of the self-partial inductance of a single circular pillar, given by (4) and the mutual partial inductance between pillars, given by (8). The expression for L_{pac} is given by (9). The net resistance of parallel circular pillars R_{pac} is half that of the single circular pillar, which is given by (10). The plot of Q_{dc} versus radius is shown in Fig. 15(a).

$$M(l, p) = \frac{\mu_0 l}{2\pi} \left[\ln \left(\frac{2l}{p} \right) - 1 \right] \quad (8)$$

where l is the length of a conductor (a pillar or an interconnect) and p is the center-to-center distance between conductors (pillars or interconnects).

$$L_{pac} = 0.5 \left(L_{circ}(l_{cp}, r) + M(l_{cp}, p) \right) \quad (9)$$

$$R_{pac} = 0.5 R_{circ}(l_{cp}, r) \quad (10)$$

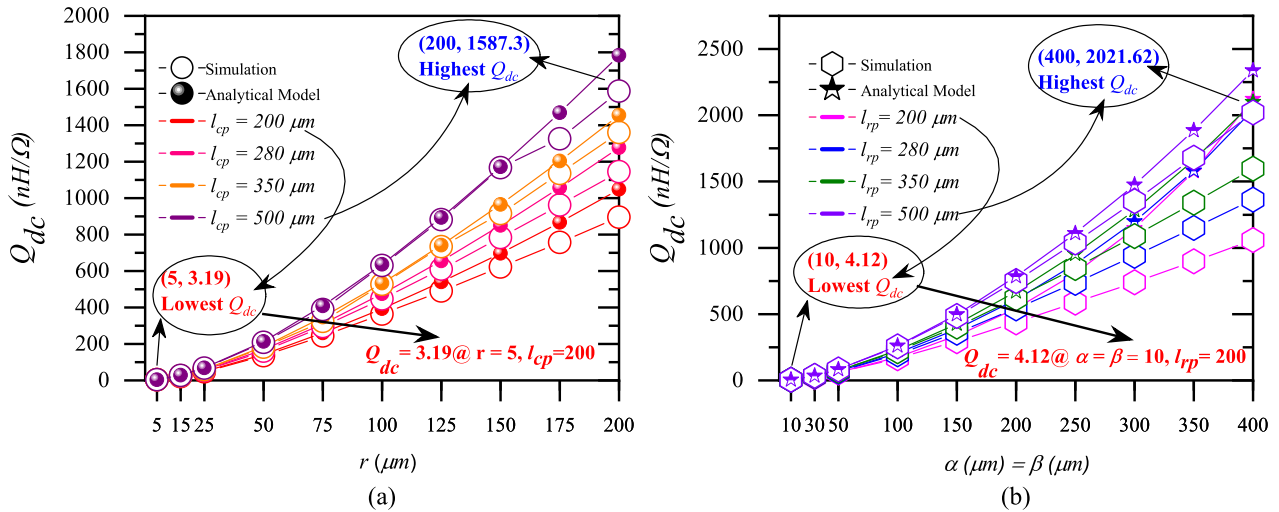


FIGURE 14. Variation of Q_{dc} of a single-pillar for different dimensions for four different lengths of pillars. (a) Circular pillar and (b) Rectangular pillar. The lowest and highest Q_{dc} values labeled on the graphs are from FEA simulations, not from analytical models.

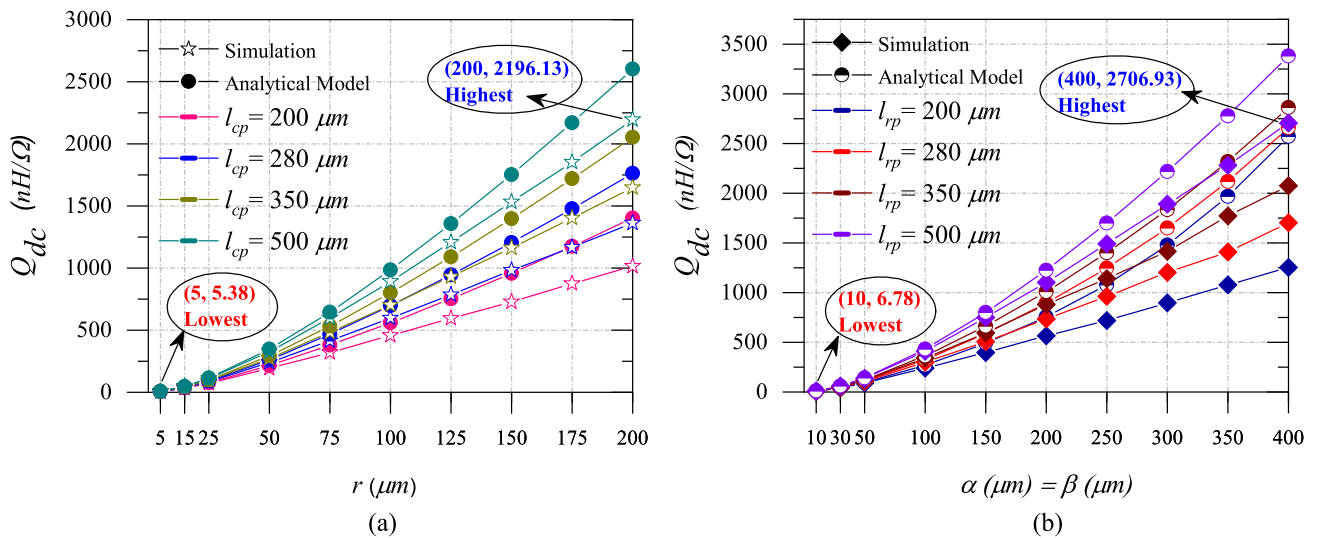


FIGURE 15. Variation of Q_{dc} of two parallel pillars for different dimensions for four different lengths of pillars. (a) Parallel circular pillars and (b) Parallel rectangular pillars.

The gap between two parallel pillars is assumed to be $5 \mu m$, which is determined from the critical dimension (CD) [50]. It should be mentioned that the equation in [50] is a first approximation. As reported in [51], the CD is a function of pillar length, photoresist chemistry, the exposure dose and the photomask feature geometry/size, wherein diffraction effects are very significant for rectangular/circular pillars.

2) TWO PARALLEL RECTANGULAR PILLARS

Similar to the previous case, the inductance L_{par} and resistance R_{par} for two parallel rectangular pillars are given by (11) and (12), respectively. The plot of Q_{dc} versus length and width is shown in Fig. 15(b).

$$L_{par} = 0.5 \left(L_{rect}(l_{rp}, \alpha, \beta) + M(l_{rp}, p) \right) \quad (11)$$

$$R_{par} = 0.5 R_{rect}(l_{rp}, \alpha, \beta) \quad (12)$$

Observation 4: The Q_{dc} of parallel pillars is greater than a single pillar. This is true for circular and rectangular pillars.

Observation 5: The Q_{dc} of parallel rectangular pillars is 23.25-26.02% higher than parallel circular pillars for approximately the same footprint. The comparisons are made at lowest ($r = 5 \mu m, \alpha = \beta = 10 \mu m, l_{cp}/r_p = 200 \mu m$) and highest ($r = 200 \mu m, \alpha = \beta = 400 \mu m, l_{cp}/r_p = 500 \mu m$) Q_{dc} values.

E. Q_{dc} OF A THREE-QUARTER-TURN

1) THREE-QUARTER-TURN WITH CIRCULAR PILLARS

The schematic of a three-quarter-turn with circular pillars is shown in Fig. 12(a). The inductance of a three-quarter-turn with circular pillars, $L_{0.75TCP}$, is equal to the sum of the self-inductances of the pillars plus the self-inductance of the interconnect minus twice the mutual inductance between the pillars and is given by (13). The

mutual inductance between a pillar and an interconnect is assumed to be zero as the magnetic fluxes produced by them are orthogonal to each other. The DCR of a three-quarter-turn with circular pillars, $R_{0.75TCP}$, is given by (14). Variation of Q_{dc} of a three-quarter-turn with circular pillars versus pitch for four different lengths of pillars is shown in Fig. 16.

$$L_{0.75TCP} = 2L_{circ}(l_{cp}, r) + L_{rect}(l_{in}, \alpha, \beta) - 2M(l_{cp}, p) \quad (13)$$

$$R_{0.75TCP} = 2R_{circ}(l_{cp}, r) + R_{rect}(l_{in}, \alpha, \beta) \quad (14)$$

2) THREE-QUARTER-TURN WITH RECTANGULAR PILLARS

The schematic of a three-quarter-turn with rectangular pillars is shown in Fig. 12(b). Similar to the previous case, the inductance ($L_{0.75TRP}$) and resistance ($R_{0.75TRP}$) for a 0.75-turn with rectangular pillars are given by (15) and (16), respectively. Variation of Q_{dc} of a three-quarter-turn with rectangular pillars versus pitch for four different lengths of pillars is shown in Fig. 17.

$$L_{0.75TRP} = 2L_{rect}(l_{rp}, \alpha, \beta) + L_{rect}(l_{in}, \alpha, \beta) - 2M(l_{rp}, p) \quad (15)$$

$$R_{0.75TRP} = 2R_{rect}(l_{rp}, \alpha, \beta) + R_{rect}(l_{in}, \alpha, \beta) \quad (16)$$

Observation 6: The Q_{dc} of 0.75-turns with circular and rectangular pillars increases with pitch. The increment with pitch ($p = 200 \mu\text{m}$ to $p = 2000 \mu\text{m}$) is 68.24-155.40% for circular pillars and 52.46-145.28% for rectangular pillars. The lowest and highest values in the range correspond to radii $5 \mu\text{m}$ and $50 \mu\text{m}$, respectively, for circular pillars and $\alpha = \beta = 10 \mu\text{m}$ and $\alpha = \beta = 100 \mu\text{m}$, respectively, for rectangular pillars. The length considered for comparison is $500 \mu\text{m}$.

Observation 7: The Q_{dc} of a 0.75-turn does not vary significantly with pillar length. The increment from $l_{cp/rp} = 200 \mu\text{m}$ to $l_{cp/rp} = 500 \mu\text{m}$ is 4.01% ($r = 5 \mu\text{m}$, $p = 200 \mu\text{m}$) and 6.38% ($r = 50 \mu\text{m}$, $p = 2000 \mu\text{m}$) in the case of circular pillars and 6.56% ($\alpha = \beta = 10 \mu\text{m}$, $p = 200 \mu\text{m}$) and 3.14% ($\alpha = \beta = 100 \mu\text{m}$, $p = 2000 \mu\text{m}$) in the case of rectangular pillars.

Observation 8: The Q_{dc} of 0.75-turn with rectangular pillars is 10.84-17.59% higher than with circular pillars. The comparison is made at the lowest ($r = 5 \mu\text{m}$, $\alpha = \beta = 10 \mu\text{m}$, $l_{cp/rp} = 200 \mu\text{m}$, $p = 200 \mu\text{m}$) and highest ($r = 50 \mu\text{m}$, $\alpha = \beta = 100 \mu\text{m}$, $l_{cp/rp} = 500 \mu\text{m}$, $p = 2000 \mu\text{m}$) Q_{dc} values.

F. Q_{dc} OF A FULL-TURN

1) FULL-TURN WITH CIRCULAR PILLARS

The schematic of a full-turn with circular pillars is shown in Fig. 12(c). The inductance of a full-turn with circular pillars, L_{TCP} , is the sum of the self and mutual inductances of and between conductors (pillars and interconnects). As previously mentioned, the mutual inductance between a pillar and an interconnect is assumed to be zero as the magnetic fluxes produced by them are orthogonal to each other. The expression for L_{TCP} is given by (17), where $l_{cp} + \beta$ is the center-to-center distance between the top and bottom interconnects.

The sign of mutual inductance is negative as the currents flow in opposite directions. The DCR of a full-turn with circular pillars, R_{TCP} , is given by (18). Variation of Q_{dc} of a full-turn with circular pillars versus pitch for four different lengths is shown in Fig. 18.

$$L_{TCP} = 2L_{circ}(l_{cp}, r) + 2L_{rect}(l_{in}, \alpha, \beta) - 2M(l_{cp}, p) - 2M(l_{in}, l_{cp} + \beta) \quad (17)$$

$$R_{TCP} = 2R_{circ}(l_{cp} + \beta, r) + 2R_{rect}(l_{in}, \alpha, \beta) \quad (18)$$

2) FULL-TURN WITH RECTANGULAR PILLARS

The schematic of a full-turn with rectangular pillars is shown in Fig. 12(d). Similar to the previous case, the inductance (L_{TRP}) and resistance (R_{TRP}) for a full-turn with rectangular pillars are given by (19) and (20), respectively. Variation of Q_{dc} of a full-turn with rectangular pillars versus pitch for four different lengths is shown in Fig. 19.

$$L_{TRP} = 2L_{rect}(l_{rp}, \alpha, \beta) + 2L_{rect}(l_{in}, \alpha, \beta) - 2M(l_{rp}, p) - 2M(l_{in}, l_{rp} + \beta) \quad (19)$$

$$R_{TRP} = 2R_{rect}(l_{rp} + \beta, \alpha, \beta) + 2R_{rect}(l_{in}, \alpha, \beta) \quad (20)$$

Observation 9: The Q_{dc} of a full-turn with circular and rectangular pillars increase with pitch. The increment in Q_{dc} with pitch ($p = 200 \mu\text{m}$ to $p = 2000 \mu\text{m}$) is 44.37-109.57% (e.g., $((246.68-117.71)/117.71)*100 = 109.57$) for circular pillars and 31.88-102.94% for rectangular pillars. The length ($l_{cp/rp}$) considered for the calculation is $500 \mu\text{m}$. Similar calculations can be carried out for other lengths.

Observation 10: The Q_{dc} of a full-turn with circular and rectangular pillars increases with pillar lengths. The increment in Q_{dc} from $l_{cp/rp} = 200 \mu\text{m}$ to $l_{cp/rp} = 500 \mu\text{m}$ is 8.33% ($r = 5 \mu\text{m}$, $p = 200 \mu\text{m}$) and 29.85% ($r = 50 \mu\text{m}$, $p = 2000 \mu\text{m}$) in the case of circular pillars and 12.96% ($\alpha = \beta = 10 \mu\text{m}$, $p = 200 \mu\text{m}$) and 35.45% ($\alpha = \beta = 100 \mu\text{m}$, $p = 2000 \mu\text{m}$) in the case of rectangular pillars.

Observation 11: The Q_{dc} of a full-turn with rectangular pillars is 4.61- 11.21% greater than a full-turn with circular pillars for the same footprint (approximately), pitch and length. The comparisons are made at the lowest ($r = 5 \mu\text{m}$, $\alpha = \beta = 10 \mu\text{m}$, $l_{cp/rp} = 200 \mu\text{m}$, $p = 200 \mu\text{m}$) and highest ($r = 50 \mu\text{m}$, $\alpha = \beta = 100 \mu\text{m}$, $l_{cp/rp} = 500 \mu\text{m}$, $p = 2000 \mu\text{m}$) Q_{dc} values.

From the DSE, we can draw two important conclusions:

- (i) The Q_{dc} of 0.75-turns is higher than a full-turn irrespective of the pillar cross section (circular or rectangular): 3.84-32.47% in the case of circular pillars and 9.79-40.36% in the case of rectangular pillars. The comparisons are made at the lowest ($r = 5 \mu\text{m}$, $\alpha = \beta = 10 \mu\text{m}$, $l_{cp/rp} = 200 \mu\text{m}$, $p = 200 \mu\text{m}$) and highest ($r = 50 \mu\text{m}$, $\alpha = \beta = 100 \mu\text{m}$, $l_{cp/rp} = 500 \mu\text{m}$, $p = 2000 \mu\text{m}$) Q_{dc} values.
- (ii) As the pillar aspect ratio increases, the analytical models results are in good agreement with the simulation results.

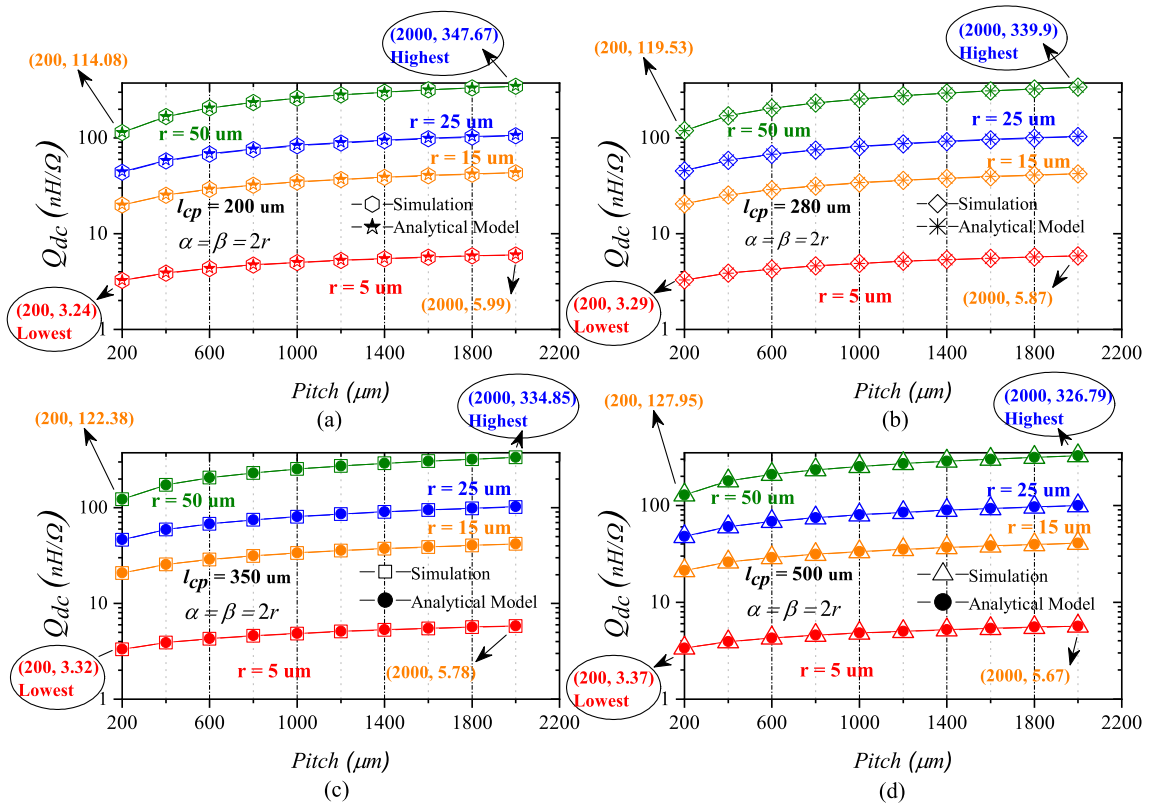


FIGURE 16. Variation of Q_{dc} of a three-quarter-turn with circular pillars versus pitch for four different lengths of pillar: (a) $l_{cp} = 200 \mu\text{m}$, (b) $l_{cp} = 280 \mu\text{m}$, (c) $l_{cp} = 350 \mu\text{m}$, and (d) $l_{cp} = 500 \mu\text{m}$. The data points marked on the graphs are from a FEA simulation.

The results of the above study demonstrate that the Q_{dc} of 3-D inductors can be improved by increasing (a) the cross-sections of the pillars and the interconnects (b) the length of the pillar (height of the inductor), and (c) the pitch of opposite current carrying pillars. Also, the study shows that 0.75-turns with rectangular pillars achieves the highest Q_{dc} . Even though 0.75-turns with rectangular pillars exhibit a better Q_{dc} than with circular pillars, 0.75-turns with circular pillars is chosen for constructing a novel inductor structure, which is discussed in the next section, for the following reasons: (a) the stress profile of a circular pillar is better than a rectangular pillar [52], [53], and (b) constructing rectangular pillars with a high aspect ratio is difficult.

III. 3-D SPIRAL INDUCTOR WITH MAGNETIC THIN-FILMS A. INDUCTOR DESIGN

From the DSE that has been discussed in the previous section, we introduce a novel 3-D spiral inductor structure with magnetic thin-films, as shown in Fig. 20. The top view of the structure is shown in Fig. 21. The features of the proposed inductor structure are described as follows:

- (i) There are N windings connected in series. Each winding consists of four 0.75 – turns, and each 0.75 – turn is comprised of two pillars, and an interconnect, as shown in Fig. 20.

- (ii) The pillars of the windings are placed along x and y axes. The distance between two consecutive pillars along the axes is S , as shown in Fig. 22.
- (iii) Energy stored in the proposed inductor is in two forms: air-core energy and magnetic-core energy. Interconnects contribute significantly to the air-core energy while contributing negligibly small to the magnetic-core energy. On the other hand, pillars contribute significantly to the magnetic-core energy while contributing negligibly small to the air-core energy. To simplify the analysis, we can consider an ideal situation where interconnects contribute 100% to the air-core energy, and pillars contribute 100% to the magnetic energy.
- (iv) The energy storage volume can be segmented into four quadrants, and the magnetic field is along the radial direction, illustrated in Fig. 21. The magnetic fields due to pillars in opposite quadrants nearly cancel each other; that is, the magnetic fields in the first and third quadrants, as well as the second and fourth quadrants, are in opposite directions. The H -fields which are immediately around the copper pillars do not get completely cancelled. Consequently, the B – field lines due to the pillars can be enhanced by wrapping high permeability magnetic materials around the pillars, which contributes to the inductance. Also, wrapping the thin-films immediately around the pillars offers a low reluctance path,

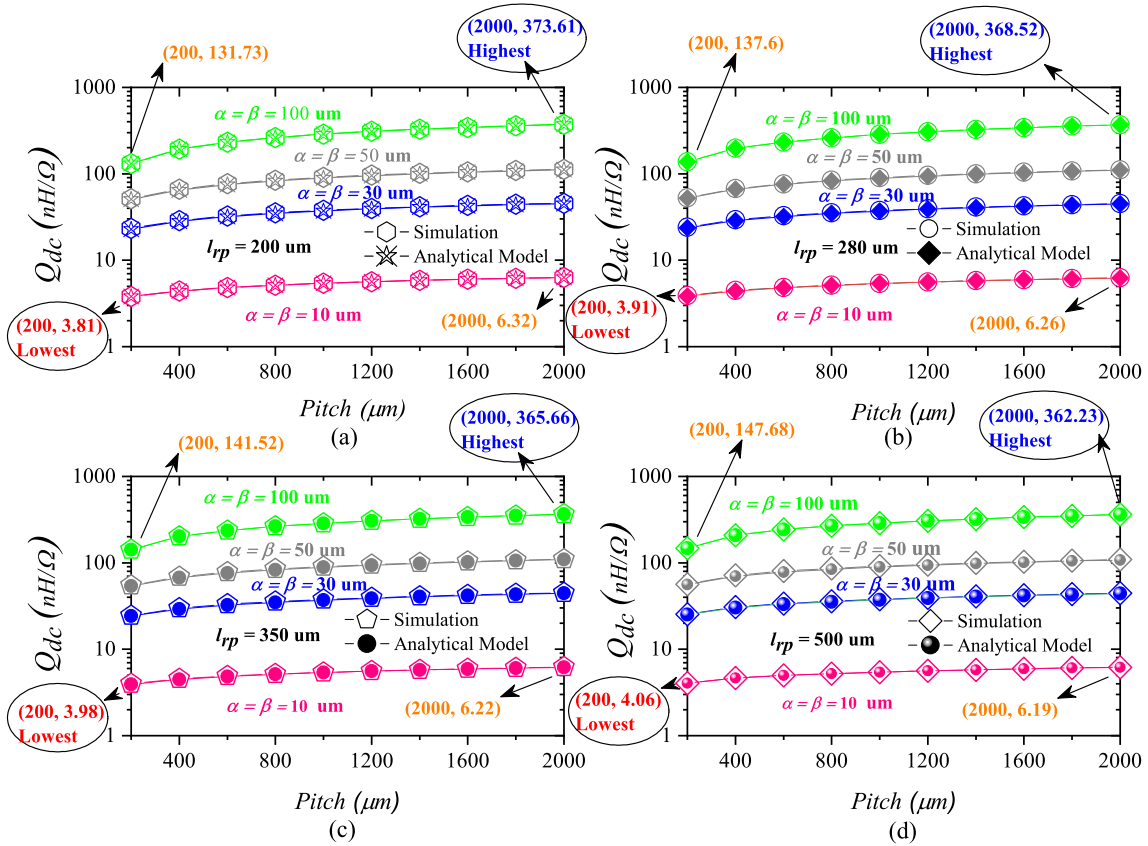


FIGURE 17. Variation of Q_{dc} of a three-quarter-turn with rectangular pillars versus pitch for four different lengths of pillars: (a) $l_{rp} = 200 \mu\text{m}$, (b) $l_{rp} = 280 \mu\text{m}$, (c) $l_{rp} = 350 \mu\text{m}$, and (d) $l_{rp} = 500 \mu\text{m}$.

and hence, improved inductance density. The basic idea here is to make use of strong magnetic field lines near the pillars. The integration of magnetic thin-films is discussed in section IV.

- (v) The pillars contribute to inductance ideally without introducing substrate loss for two reasons: (a) the H -field direction is parallel to the substrate plane, and (b) most of the H -fields due to the pillars cancel each other in the substrate volume.
- (vi) In the proposed inductor, approximately 75% and 25% of the total inductance are contributed by air-core (due to the interconnects) and magnetic-core (due to the pillars), respectively.

Even though larger cross-section windings yield higher Q_{dc} , we have chosen $100 \mu\text{m}$ diameter pillars and $100 \mu\text{m} \times 100 \mu\text{m}$ interconnects as it is challenging to fabricate windings thicker than $100 \mu\text{m}$ [17], [51]. Increasing the conductor dimensions will lower the DC resistance, but this results in a longer reluctance path (longer flux path) and in turn a reduction in flux density. The windings and thin-film magnetic-cores are strategically arranged to increase the field strength.

B. SERIES INDUCTANCE OF THE WINDING

We derive an analytical expression for the winding inductance (air-core inductance) of the 3-D spiral inductor structure.

We make use of the basic formulas given in Appendix A. The inductance of this inductor structure is the summation of the self-inductances of all N -windings and the mutual inductances between all pairs of windings. The physical structure used to compute the inductance is shown in Fig. 22. To simplify the process of analytical modelling, the windings are assumed to be completely closed, and each winding is excited separately [54]. The current direction in all windings is the same: either clockwise or anticlockwise.

The dc winding inductance $L_{w,dc}$ of the novel inductor with N windings can be expressed as follows:

$$L_{w,dc} = \sum_{i=1}^N L_{w_i} + 2 \sum_{j=i+1}^N \sum_{i=1}^{N-1} M_{w_i-w_j} \quad (21)$$

The first term, L_{w_i} , corresponds to the self-inductance of the i th winding. The second term, $M_{w_i-w_j}$, represents the mutual inductance between the i th and j th windings.

The self-inductance of the i th winding is given by

$$L_{w_i} = 4L_{circ}(l_{cp}, r) + 4L_{rect}(\sqrt{2}iS, \alpha, \beta) + 4M(l_{cp}, 2iS) - 8M(l_{cp}, \sqrt{2}iS) - 4M(\sqrt{2}iS, \sqrt{2}iS) \quad (22)$$

Similarly, the mutual inductance between the i th and j th windings is

$$M_{w_i-w_j} = 4 \left(M(l_{cp}, (j-i)S) - 2M(l_{cp}, \sqrt{(i^2 + j^2)S}) \right)$$

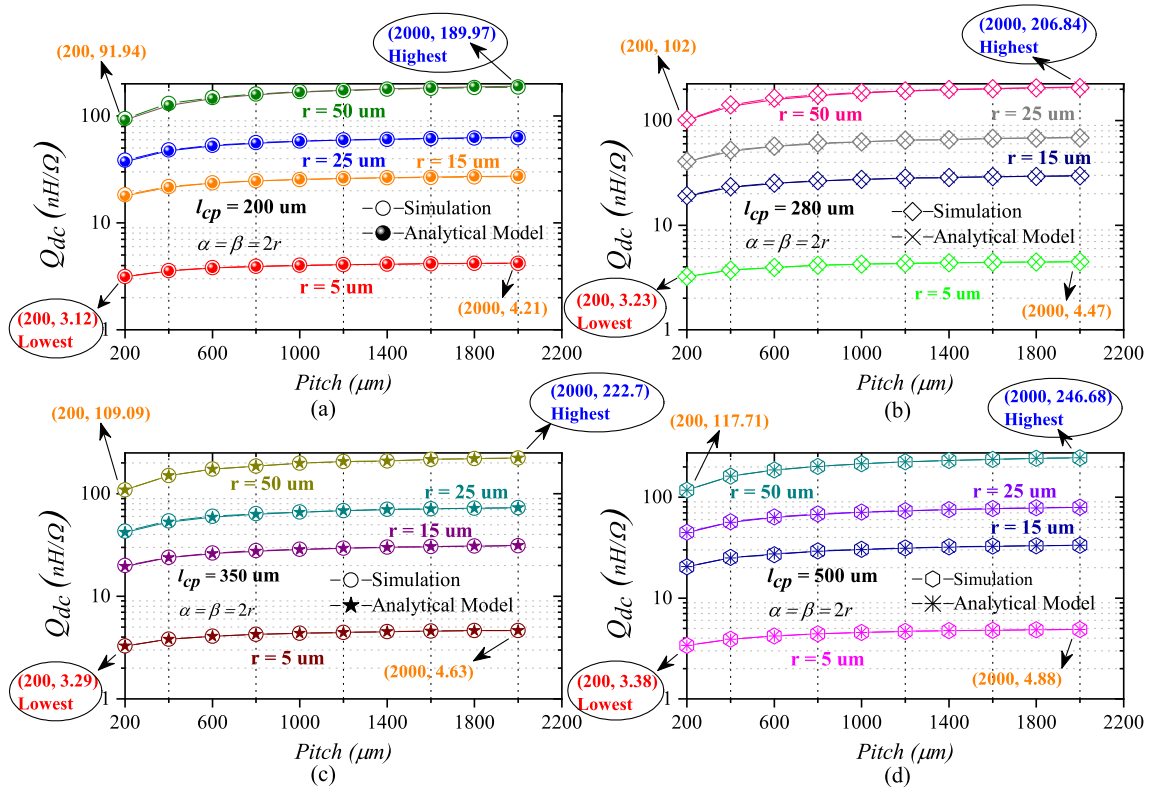


FIGURE 18. Variation of Q_{dc} of a full-turn with circular pillars versus pitch for four different lengths of pillars: (a) $l_{cp} = 200 \mu\text{m}$, (b) $l_{cp} = 280 \mu\text{m}$, (c) $l_{cp} = 350 \mu\text{m}$, and (d) $l_{cp} = 500 \mu\text{m}$.

$$\begin{aligned}
 &+ M(l_{cp}, (i + j)S) \\
 &+ M\left(\left(\frac{j-i}{\sqrt{2}}\right)S + \sqrt{2}iS, \left(\frac{j-i}{\sqrt{2}}\right)S\right) \\
 &- M\left(\left(\frac{j-i}{\sqrt{2}}\right)S, \left(\frac{j-i}{\sqrt{2}}\right)S\right) \\
 &- M\left(\left(\frac{j-i}{\sqrt{2}}\right)S + \sqrt{2}iS, \left(\frac{i+j}{\sqrt{2}}\right)S\right) \\
 &+ M\left(\left(\frac{j-i}{\sqrt{2}}\right)S, \left(\frac{i+j}{\sqrt{2}}\right)S\right) \quad (23)
 \end{aligned}$$

The basic idea of the computations of the self and mutual inductances of and between the windings (i.e., L_{w_i} and $M_{w_i-w_j}$) are summarized in Appendix II and Appendix III, respectively.

In the derivation of (21), the following assumptions have been made:

- (i) The substrate resistivity is very high. The eddy current effect is not present in the silicon substrate at high frequency (i.e., the eddy currents do not alter the flux distribution).
- (ii) A thin-film magnetic-core is not present.
- (iii) The current is distributed uniformly in the conductor; that is, the skin and proximity effects are not present.

Next, we consider high-frequency effects, such as the skin effect, on the inductance. The proximity effect, which is one of the high-frequency effects, is not considered for the reason

explained in the next section. Due to the skin effect, the high-frequency current tends to be crowded in an annulus (thickness equal to the skin depth) at the surface of the conductor. Consequently, no internal current is linked by the field. As $f \rightarrow \infty$, the internal inductance vanishes (i.e., $L_{in} \rightarrow 0$). The inductance value with the skin effect is given by the following equation:

$$L_{w,ac} = L_{w,dc} - L_{in} \quad (24)$$

where L_{in} is the internal inductance of the proposed inductor. The expression for L_{in} is given by

$$L_{in} = 4 \left(NL_{circ,in}(l_{cp}) + \sum_{i=1}^N L_{rect,in}(\sqrt{2}iS, \alpha, \beta) \right) \quad (25)$$

In the frequency range of 3-30 MHz, the skin depth is very high, and hence, the effect of skin effect on the winding inductance is negligibly small. Consequently, the AC winding inductance is approximately equal to DC winding inductance, that is, $L_{w,ac} \approx L_{w,dc}$.

Equation (21) does not consider the inductance contribution from thin-film magnetic-cores. The integration of magnetic thin-films into the proposed inductor structure and the analytical model for the inductance due to the magnetic thin-films are discussed in section IV.

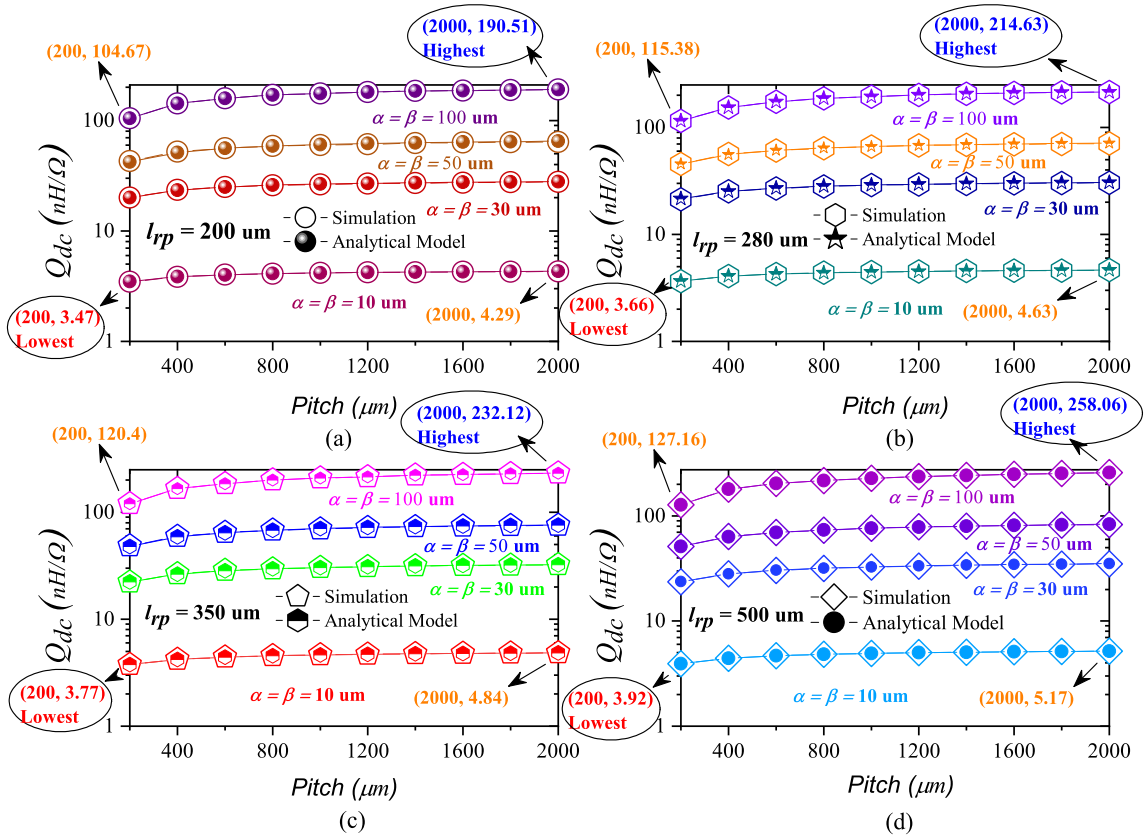


FIGURE 19. Variation of Q_{dc} of a full-turn with rectangular pillars versus pitch for four different lengths of pillars: (a) $l_{pp} = 200 \mu\text{m}$, (b) $l_{pp} = 280 \mu\text{m}$, (c) $l_{pp} = 350 \mu\text{m}$, and (d) $l_{pp} = 500 \mu\text{m}$.

C. SERIES RESISTANCE OF THE WINDING ($R_{w,ac}$)

The AC resistance of the inductor winding is caused by the skin and proximity effects. The proximity effect is not pronounced when the conductors are placed far apart in the frequency range of 3-30 MHz. The center-to-center distance between conductors should be more than four conductor radii [55]. Moreover, it's analytically difficult to determine the ac resistance due to the proximity effect. In the case of the proposed inductor, the center-to-center distance between the conductors varies from 175 to 250 μm. Consequently, we can safely ignore the resistance due to the proximity effect. The only resistance that needs to be considered is the skin effect resistance. The AC resistance of the pillars and interconnects due to the skin effect are expressed by (26) and (27), respectively.

$$R_{circ,skin} = \frac{2}{\delta} \left(NrR_{circ}((l_{cp} + \beta), r) \right) \tag{26}$$

$$R_{rect,skin} = \frac{2}{\delta} \left(\left(\frac{\alpha\beta}{\alpha + \beta} \right) \sum_{i=1}^N R_{rect}(\sqrt{2iS}, \alpha, \beta) \right) \tag{27}$$

The effective area for the flow of current decreases due to the skin effect, and the effective area is obtained by multiplying the skin depth by the circumference of the conductor; this is applicable for both rectangular as well as circular cross-

section conductors. The skin depth, δ , can be expressed as

$$\delta = \sqrt{\frac{\rho}{\pi f \mu}} \tag{28}$$

where f is the operating frequency, ρ is the resistivity, and μ is the permeability. The permeability can be written as the product of the relative permeability μ_r and the permeability of free space, $\mu_o = 4\pi \times 10^{-7} \text{H/m}$: $\mu = \mu_o \mu_r$.

The high frequency resistance of pillars and interconnects, derived in [56], is given by (29) and (30), respectively.

$$R_{w,circ} = \sqrt{R_{circ,dc}^2 + R_{circ,skin}^2} \tag{29}$$

$$R_{w,rect} = \sqrt{R_{rect,dc}^2 + R_{rect,skin}^2} \tag{30}$$

where $R_{circ,dc}$ and $R_{rect,dc}$ are given by (31) and (32), respectively.

$$R_{circ,dc} = 4NR_{circ}((l_{cp} + \beta), r) \tag{31}$$

$$R_{rect,dc} = 4 \sum_{i=1}^N R_{rect}(\sqrt{2iS}, \alpha, \beta) \tag{32}$$

Finally, the series resistance of winding ($R_{w,ac}$) is given by (33).

$$R_{w,ac} = R_{w,circ} + R_{w,rect} \tag{33}$$

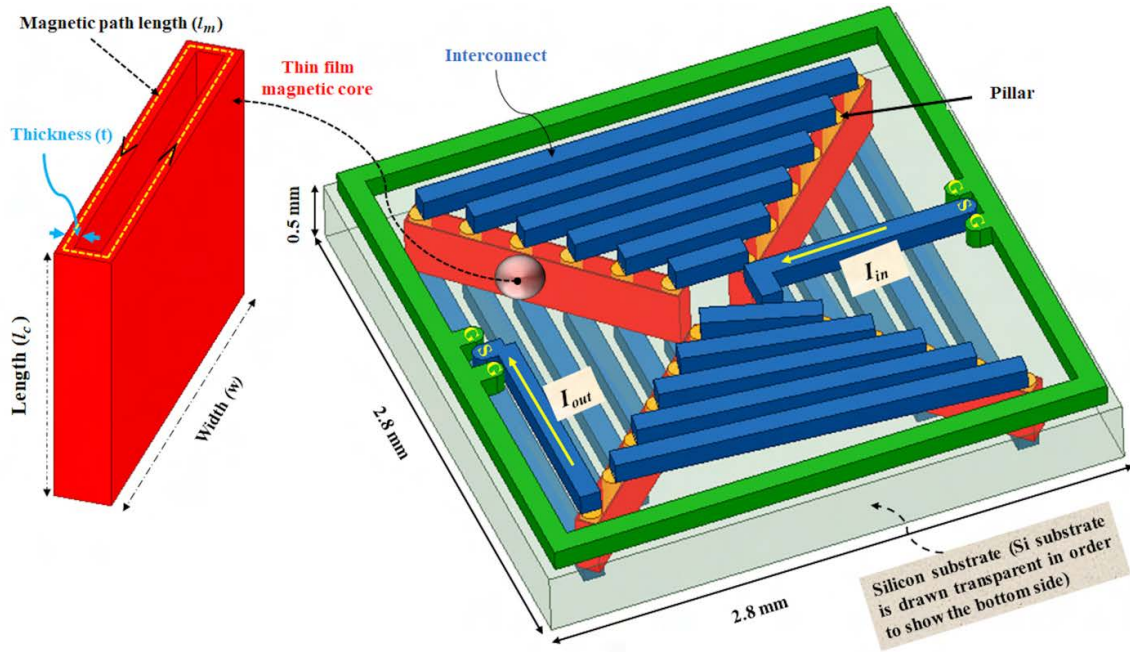


FIGURE 20. Physical structure of the 3-D spiral inductor structure with a thin-film magnetic-core.

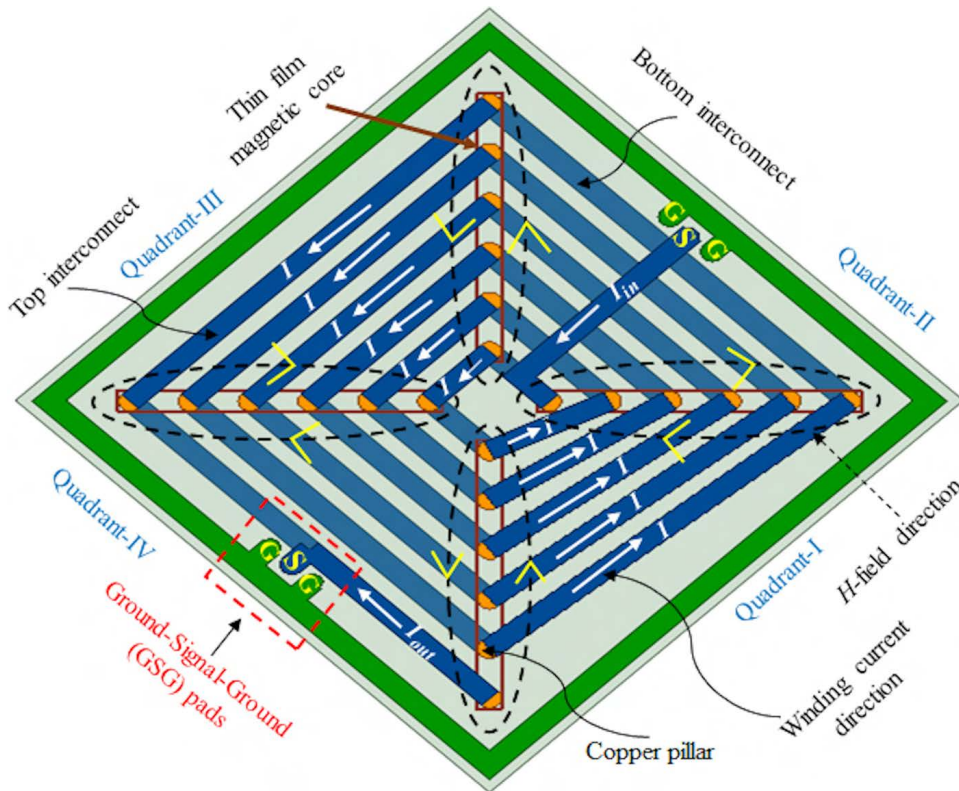


FIGURE 21. Top view of the 3-D spiral inductor structure with magnetic thin-films.

IV. INTEGRATION OF MAGNETIC THIN-FILMS

A. DESCRIPTION

The proposed inductor with magnetic thin-films is shown in Fig. 20. $Co - Zr - Ta - B$ thin-films are considered here. We have employed single-layer magnetic thin-films, which

are wrapped around the pillars. The magnetic thin-films are placed parallel to the $x - z$ plane or the $y - z$ plane. The plane of the magnetic thin-films is placed parallel to the H -field (magnetic field strength). The H -field is in the x or the y direction, and the eddy current flows in the z -direction. The

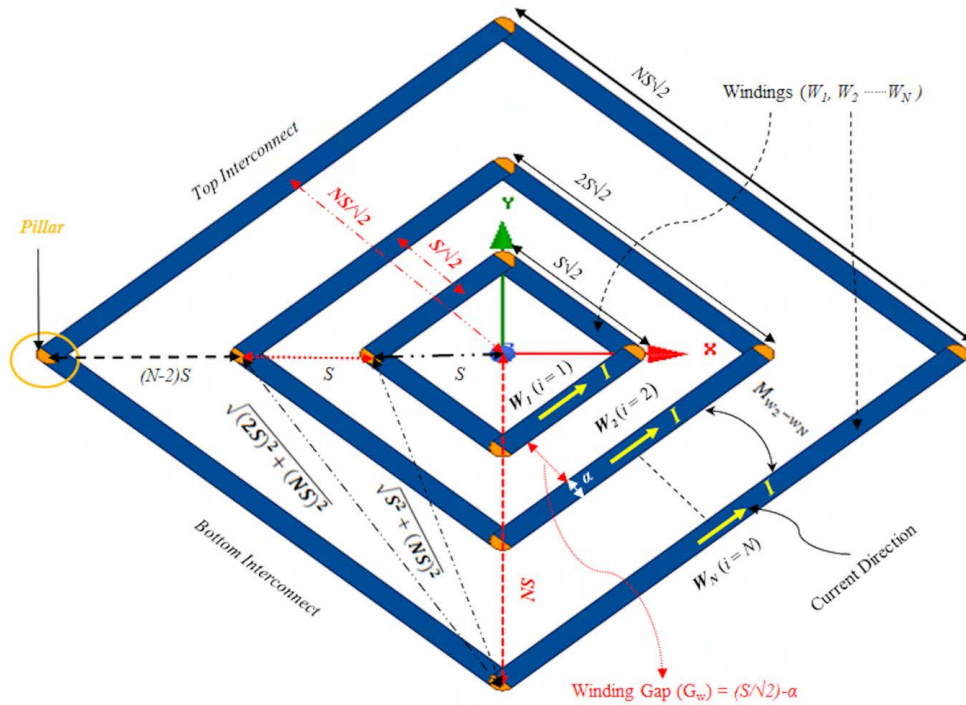


FIGURE 22. Top view of the physical structure considered for computing the series inductance of the winding, where the windings are assumed to be completely closed and each winding is excited separately.

hard axis is assumed to be along the direction of the H -field, x and y axes, and the easy axis is assumed to be oriented in the pillar current direction (z -axis). The dimensions of the thin-film magnetic-core are as follows: $500 \mu\text{m}$ in length (l_c), $1364 \mu\text{m}$ in width (w), and the thickness (t) is $1 \mu\text{m}$.

B. FABRICATION METHOD

The inductor structure, as shown in Fig. 20, can be fabricated by the following method, as shown in Fig. 23: (1) form trenches parallel to the x and y axes in a Si substrate with deep reactive ion etching (DRIE) or laser ablation, wherein if DRIE is used, sidewall scalloping can be reduced by implementing a short etch cycle duration and/or using a selective Si wet etch since the kinetics are a function of surface area, (2) selectively deposit a $1 \mu\text{m}$ thick magnetic-core (e.g., NiFe) in the trenches using a non-line of sight deposition technique such as electroless plating by way of a Pd^{2+} electroless plating catalyst adhered to a (3-aminopropyl) triethoxysilane (APTES) self-assembled monolayer (SAM) that is further adhered to oxygen plasma (or thermally) treated Si [57], wherein in addition to shape anisotropy, an external magnetic field directed orthogonal to the substrate during electroless deposition could be used to establish a vertically oriented easy axis, (3) attach a $100 \mu\text{m}$ thick Cu carrier wafer to the Si substrate, (4) pattern the trenches using an in-situ photomask method, wherein an aspect ratio of 10 is feasible with a standard g-, h-, i-line mask aligner [58] and use bottom-up electroplating to form the Cu pillars, (5) protect the deposited materials with a thin layer of photoresist

then pattern and selectively etch the Cu carrier wafer to form the backside RDL, and (6) implement standard lithography/electroplating on the front side to form the 2^{nd} RDL layer, which can include the GSG traces.

C. LOSS MECHANISM

The main loss mechanisms involved in magnetic thin-films are hysteresis loss, eddy current loss, and anomalous loss [5]. The eddy current loss can be classified as conduction eddy current loss and displacement eddy current loss. Multi-layer film stacks (multi-layer magnetic thin-films) are the source of displacement eddy current loss. In the case of single-layer magnetic thin-film, displacement eddy current loss is absent. Consequently, the losses associated with the single-layer magnetic thin-film are hysteresis loss, conduction eddy current loss, and anomalous loss.

The thickness of each layer used in 3-D spiral inductor structure is $1 \mu\text{m}$, which is much less than one skin depth at 30 MHz. The skin depth of $Co - Zr - Ta - B$ is $5 \mu\text{m}$ at 30 MHz. The measured relative permeability considered for the skin depth calculation is 500, and the resistivity of $Co - Zr - Ta - B$ is $115 \mu\Omega \cdot \text{cm}$.

D. INDUCTANCE OF MAGNETIC THIN-FILMS

The inductance due to magnetic thin-films can be derived using a basic magnetic circuit approach. The flux ϕ_{mag} in the thin-film magnetic-core is given by

$$\phi_{mag} = \frac{\text{Magnetomotive Force}}{\text{Reluctance}} = \frac{NI}{\mathcal{R}_{mag}} \quad (34)$$

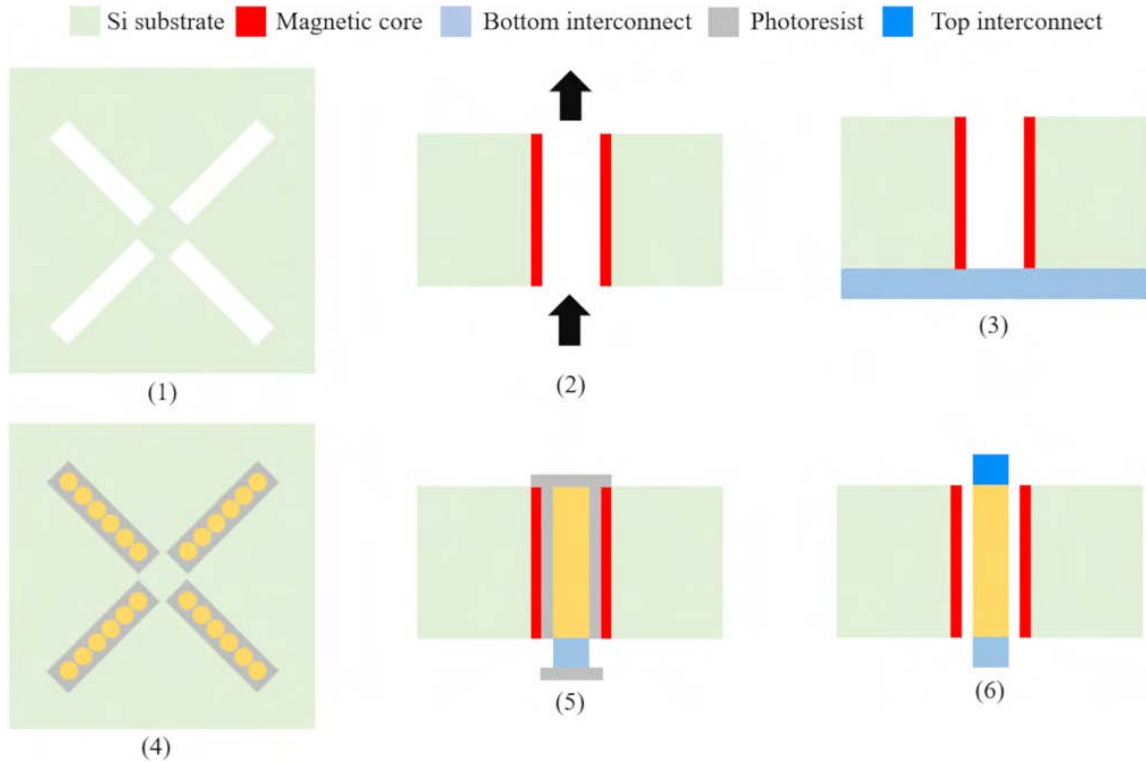


FIGURE 23. Process schematic for the spiral inductor structure with a thin-film magnetic-core, as corresponds to Fig. 20. (1) Inductor top-down view. Trenches are formed through the substrate by DRIE or laser ablation. (2) Trench cross-section. An external magnetic field is applied orthogonal to the substrate surface whilst a magnetic-core is conformally deposited in the trenches by electroless deposition (SiO_2 , SAM and Pd^{2+} catalyst layers not shown). (3) A Cu carrier wafer is bonded to the substrate backside and the bonding material is etched from the trench bottom (bonding layer not shown). (4) Inductor top-down view. A photoresist is patterned in the trenches using an in situ photomask, which enables high aspect ratio mold creation, and the Cu pillars are bottom-up electroplated. (5) Trench cross-section. A photoresist protects the topside deposited material and is also used as a pattern for a selective Cu etch to form the bottom interconnect (BIC) (interconnect in/out of the page). The backside photoresist is shown overhanging the BIC due to an isotropic wet etch. (6) The top interconnect (TIC) is patterned and electroplated using standard RDL processing. To enable a stable structure for plating the TIC, the topside photoresist can be selectively removed by using different photoresists or by CMP. This would enable leaving the vertically oriented photoresist in place to act as a supporting structure before the TIC deposition.

The reluctance \mathcal{R}_{mag} of the flux path in the core can be written as:

$$\mathcal{R}_{mag} = \frac{l_m}{\mu_o \mu_r l_c t} \quad (35)$$

where l_c and t are the length and thickness of the thin-film magnetic-core, respectively, and l_m is the magnetic path length (i.e., $8r + 2(N - 1)S + 4t$), shown in Fig. 20.

The DC inductance, $L_{mag,dc}$, due to magnetic thin-films is given by

$$L_{mag,dc} = \frac{N \phi_{mag}}{I} = \frac{N^2 \mu_o \mu_r l_c t}{8r + 2(N - 1)S + 4t} \quad (36)$$

Expression (36) is derived with the assumption that the flux is uniformly distributed over the cross-section of the magnetic thin-film. This is true only for direct current or low frequency currents, but at high-frequency the flux density ceases to be uniform. Since the thickness of the magnetic thin-film is significantly less than the skin depth, the flux completely penetrates into the magnetic thin-film. In other

words, (36) can be employed to find the inductance due to thin-film magnetic-cores without appreciable error in the frequency range of 3-30 MHz; that is, $L_{mag,ac} \approx L_{mag,dc}$.

V. CHARACTERIZATION AND VALIDATION

To verify the proposed model for winding inductance, an air-core 3-D spiral inductor is implemented on PCB and electrically characterized with an HP4285A precision LCR meter (75 kHz-30 MHz). The specifications and validation results are presented in Appendix IV.

Similarly, to verify the analytical model for the inductance of magnetic thin-films and understand the potential of 3-D spiral inductors with magnetic thin-films, we constructed and characterized (small-signal) in Ansys Maxwell. The specifications considered for the simulation are given in Table 1. The resistivity of the silicon considered for the simulation is $1 \text{ k}\Omega \cdot \text{cm}$. The total DC inductance is the sum of the inductances due to the windings and the magnetic thin-films, and is given by (37).

$$L_{dc} = L_{w,dc} + L_{mag,dc} \quad (37)$$

TABLE 2. Dimensions of the 3-D spiral inductor with magnetic thin-films.

Design Parameter	Value
Number of windings (N)	6
Number of pillars in each winding	4
Distance between two pillars along the axes (S)	250 μm
Pillar radius (r)	50 μm
Interconnect width (α)	100 μm
Interconnect height (β)	100 μm
Inductor height (l_{cp})	500 μm
Winding gap (G_w) = $(S/\sqrt{2}) - \alpha$	75 μm
Thickness of magnetic thin-film (t)	1 μm

TABLE 3. Simulation and analytical model comparison.

	Simulation	Model	Percent Error (%)
$L_{w,dc}$ (nH) (air-core)	46.63	49.84	6.88
$L_{mag,dc}$ (nH) (magnetic-core)	16.43	15.56	5.29
$R_{w,ac}$ (m Ω) @3 MHz	99.26	96.8	2.47
$R_{w,ac}$ (m Ω) @10 MHz	134.09	126.7	5.51
$R_{w,ac}$ (m Ω) @20 MHz	161.13	160	0.70
$R_{w,ac}$ (m Ω) @30 MHz	188.54	187.5	0.55
R_e (m Ω) @30 MHz	94.43	-	-
R_h (m Ω) @30 MHz	49.75	-	-
Q_{ac} (m Ω) @30 MHz	36	-	-

Table 3 compares simulation and analytical results for $L_{w,dc}$ and $L_{mag,dc}$. Since the skin effect is not significant in the frequency range of 3-30 MHz, AC inductance is approximately equal to DC inductance, that is, $L_{ac}(L_{w,ac} + L_{mag,ac}) \approx L_{dc}$.

The total loss in any inductor is the sum of the winding loss and core loss [5]. As discussed in section IV, the main losses associated with single-layer magnetic thin-films are conduction eddy current loss, hysteresis loss, and anomalous loss. Since this work focuses on small-signal characterization, anomalous loss, which appears at large ac currents, is not taken into account. The losses that need to be considered in the 3-D spiral inductor with magnetic thin-films are winding loss, eddy current loss, and hysteresis loss; the resistances corresponding to these losses are represented by the winding resistance $R_{w,ac}$ [see (33)], eddy current resistance R_e , and hysteresis resistance R_h , respectively. The total resistance, R_{ac} , which is known as small-signal resistance, is given by the following equation:

$$R_{ac} = R_{w,ac} + R_e + R_h \quad (38)$$

Table 3 compares simulation and analytical results for $R_{w,ac}$. The analytical expressions for R_e and R_h are not derived as a closed form solution is difficult.

The inductor model is assumed to be comprised of inductance L_{ac} in series with resistance R_{ac} . The parasitic capacitances, such as interwinding capacitance, which significantly influence Q_{ac} at VHF, are not considered. Consequently, the

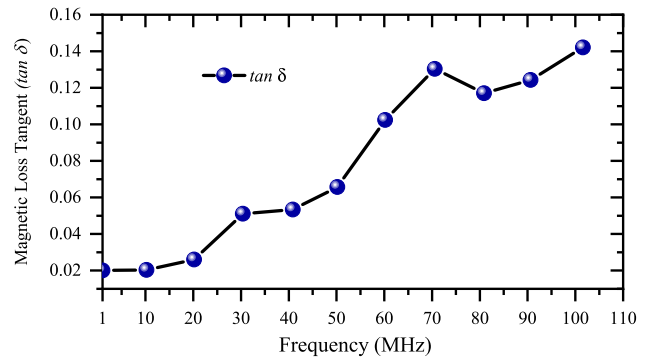


FIGURE 24. The loss tangent $\tan \delta$ versus frequency.

Q_{ac} at low frequencies can be described by $\omega L_{ac}/R_{ac}$. In this expression, ω ($2\pi f$) is the angular frequency.

The small-signal performances can be accurately evaluated using the FEA. The performance of an inductor can be evaluated using a figure-of-merit (FOM), which is defined by [5] as,

$$FOM = \frac{\sqrt{Q_{dc} \cdot Q_{ac}}}{V} \quad (39)$$

where V is the volume of the inductor. In Table 4, the FOM of the 3-D spiral inductor with magnetic thin-films and inductors from previously published works are compared.

In Table 4, for the computation of Q_{ac} ($2\pi f L_{ac}/R_{ac}$) at 30 MHz, the calculated resistances (FEA solutions) corresponding to the winding loss, eddy current loss, and hysteresis loss are 188.54 m Ω ($R_{w,ac}$), 94.43 m Ω (R_e), and 49.75 m Ω (R_h), respectively. As discussed in section V, R_{ac} is the sum of all these three resistances and is equal to 332.72 m Ω . The hysteresis loss is estimated by using magnetic loss tangent ($\tan \delta$) measured on a single-layer CZTB sample of 1 μm thickness; a sample of size 4 mm \times 4 mm \times 0.7 mm (including the silicon substrate) is considered. The measured $\tan \delta$ is 0.02 at low frequency where eddy current loss is negligibly small. The loss tangent $\tan \delta$ is plotted in Fig. 24.

VI. CONCLUSION

In this paper, we report the closed-form analytical model for the inductance of a 3-D spiral inductor with magnetic thin-films. The analytical expressions for the inductances of the winding and the magnetic thin-films are validated against measurements and FEA solutions, respectively. The values predicted by the inductance models of the winding and the magnetic thin-films agree with the experimental and FEA simulation results to within 5.63% and 5.29%, respectively.

Also, the analytical expression for the winding resistance ($R_{w,ac}$) is derived. The values predicted by the expression are validated against simulation results in the frequency range of 3-30 MHz; the maximum error reported is 5.5%, as illustrated in Table 3.

The design space is graphically described. An extensive analysis is carried out to evaluate the DC performance

TABLE 4. Small-signal performance of a 3-d spiral inductor with magnetic thin-films compared with the previously published works to demonstrate its potential for power supply applications.

Reported work	Type	Core	Footprint (mm^2)	Height (mm)	L_{dc} (nH)	R_{dc} (m Ω)	Q_{dc} (nH/ Ω)	Q_{ac} @ freq (MHz)	FOM $\frac{\sqrt{Q_{ac} \cdot Q_{dc}}}{V}$
This work *	3-D Spiral	CZTB	4.5 [§]	0.5	63.06	88.43	713.34	36@30	71.22
[59]	Bar-Type	$Ni_{81}Fe_{19}$	4 [§]	0.11	100	300	333.33	2.1@1	60.13
[60]	Toroid	$Ni_{80}Fe_{20}$	31.36 [§]	0.2	500	95	5263.16	20@2	51.72
[5]	Toroid	NiZn+PDMS	5.6 [§]	0.28	86.50	230	376	14.16@13	46.53
[61]	Racetrack	$Ni_{45}Fe_{55}$	7.48 [§]	0.17	150	191	785.34	4@8	44.07
[18]	Square-Shaped Spiral	NiZn+PDMS	9 [§]	0.83	430	84	5119.03	20.8@6	43.89
[62]	Toroid	MnZn+PDMS	2.9 [§]	0.4	43.6	280	155.71	16.2@65	43.29
[26]	Solenoid	Silicon-Steel Iron	3 [§]	1	1063	100 [†]	10630	1.31@5	39.33
[63]	2-D Spiral	NiZn+PDMS	9 [§]	0.6	390	140	2785.71	10@6	30.90
[64]	Elongated Racetrack	Ni-Cu-Zn Ferrite	22.7 [§]	1.06	242	820	295.12	18@30	3.02
[64]	Racetrack	Ni-Cu-Zn Ferrite	30 [§]	1.06	370	1060	349.05	14@30	2.19
[24]	Toroid	CoNiFe	100 [§]	1	1000	700	1428.57	18@1	1.60
[65]	Toroid	NiZn+PDMS	169 [§]	0.2	160	265	603.77	10.5@14	1.47

* FEA results are considered for comparison. The FOM value is merely a first approximation. The exact value of the FOM will depend on the capability of the fabrication processing technology.

[†] This is an estimated value based on the dimensions given in the reference.

[§] This value is the inductor footprint and does not include the footprint of measurement pads.

(i.e., Q_{dc}) of 3-D inductors with respect to variation of parameters such as winding dimensions, pitch, height, etc. The data is presented in graphical form. With the presented data, the determination of DC performance (i.e., Q_{dc}) of 3-D inductors with respect to variation of parameters is fairly easy, which helps in design and fabrication to achieve optimum performance.

We construct a 3-D spiral inductor with magnetic thin-films in Ansys Maxwell to understand its potential (small-signal performance) when compared with previously published works. We also discuss the loss mechanism associated with single-layer magnetic thin-films. Theoretically demonstrated that the inductance exhibited by the proposed inductor is large enough to operate a switching converter in continuous conduction mode in the proposed frequency (3-30 MHz) of operation. The 3-D spiral inductor with magnetic thin-films is more suitable for PwrSiP and PwrSoC in the frequency range of 3-30 MHz, however, it can be employed at VHF provided that EMI can be tolerated and further analysis at VHF is carried out.

APPENDIX I. EXACT FORMULAE FOR THE SELF AND MUTUAL PARTIAL INDUCTANCES OF AND BETWEEN CONDUCTORS HAVING CIRCULAR AND RECTANGULAR CROSS SECTIONS

The exact expression for the self-partial inductance of a circular pillar having length, l_{cp} , and radius, r , is given by

$$L_{circ}(l_{cp}, r) = \frac{\mu_o}{2\pi} \left[l_{cp} \ln \left(\frac{l_{cp} + \sqrt{l_{cp}^2 + r^2}}{r} \right) - \sqrt{l_{cp}^2 + r^2} + r \right] \quad (A.1)$$

Similarly, the exact expression for the self-partial inductance of a rectangular pillar having length, l_{rp} , width, α , and thickness, β , is given by

$$L_{rect}(l_{rp}, \alpha, \beta) = \frac{\mu_o l_{rp}}{2\pi} \left[\ln \left(\frac{2l_{rp}}{\alpha + \beta} \right) + 0.5 + \frac{\alpha + \beta}{3l_{rp}} \right] \quad (A.2)$$

Finally, the exact expression for the mutual partial inductance is given by

$$M(l, p) = \frac{\mu_o}{2\pi} \left[l \ln \left(\frac{l + \sqrt{l^2 + p^2}}{p} \right) - \sqrt{l^2 + p^2} + p \right] \quad (A.3)$$

where l is the length of a conductor (a pillar or an interconnect) and p is the center to center distance between conductors (pillars or interconnects).

APPENDIX II. COMPONENTS OF THE SELF-INDUCTANCE OF A WINDING

The constituent components of (22) are represented in Fig. 25. The signs of the mutual inductances depend on the current directions. Dots and crosses are used to indicate the pillar current directions as shown in Fig. 25.

APPENDIX III. COMPONENTS OF THE MUTUAL INDUCTANCE BETWEEN TWO WINDINGS

The individual mutual inductances of (23) are given by (C.1)-(C.5) and are represented in Fig. 26. The method for determining the mutual inductance between unequal straight segments is given in [55] and [66].

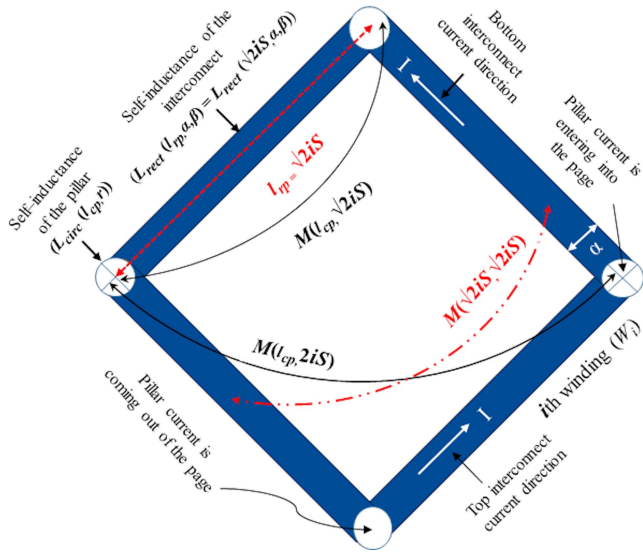


FIGURE 25. Components of the self-inductance of a winding.

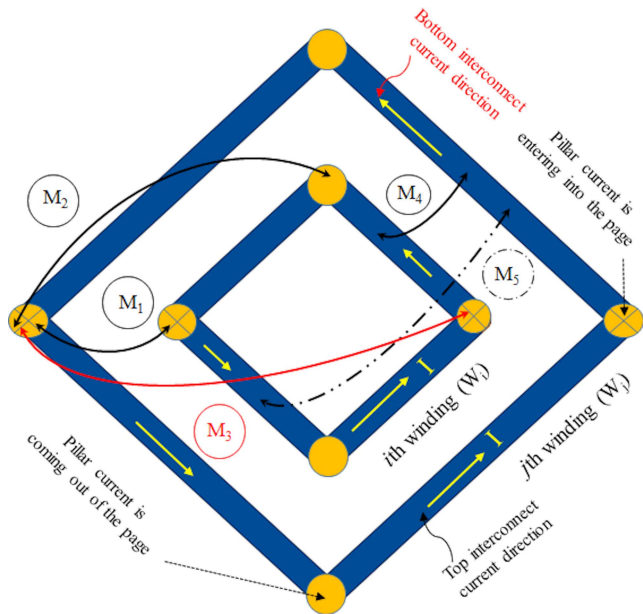


FIGURE 26. Components of the mutual inductance between two windings.

$$M_1 = M(l_{cp}, (j - i)S) \tag{C.1}$$

$$M_2 = M(l_{cp}, \sqrt{(i^2 + j^2)S}) \tag{C.2}$$

$$M_3 = M(l_{cp}, (i + j)S) \tag{C.3}$$

$$M_4 = M\left(\left(\frac{j-i}{\sqrt{2}}\right)S + \sqrt{2}iS, \left(\frac{j-i}{\sqrt{2}}\right)S\right) - M\left(\left(\frac{j-i}{\sqrt{2}}\right)S, \left(\frac{j-i}{\sqrt{2}}\right)S\right) \tag{C.4}$$

$$M_5 = M\left(\left(\frac{j-i}{\sqrt{2}}\right)S + \sqrt{2}iS, \left(\frac{i+j}{\sqrt{2}}\right)S\right) - M\left(\left(\frac{j-i}{\sqrt{2}}\right)S, \left(\frac{i+j}{\sqrt{2}}\right)S\right) \tag{C.5}$$

TABLE 5. Design parameters of the air-core 3-d spiral inductor on PCB.

Design Parameter	Value
PCB material	FR-4
Number of layers	2
Area	10 mm × 10 mm
Thickness	1 mm
Number of windings (N)	6
Number of vias in each winding	4
Distance between two vias along the axes (S)	1178.51 μm
Via radius (r)	150 μm
Copper trace width (α)	400 μm
Copper trace height (β)	35 μm

TABLE 6. Comparison of the inductance from our model, simulations, and measurements of an air-core 3-d spiral inductor on PCB.

Measurement@ frequency (kHz)	Simulation ‡ (200.85 nH)	Our Model ‡ (215.48 nH)
203.33@75	-	5.63%
202.27@100	-	6.53%
199.95@300	-	7.76%
199.07@500	-	8.24%

‡ DC inductance $L_{w,dc}$ is presented.

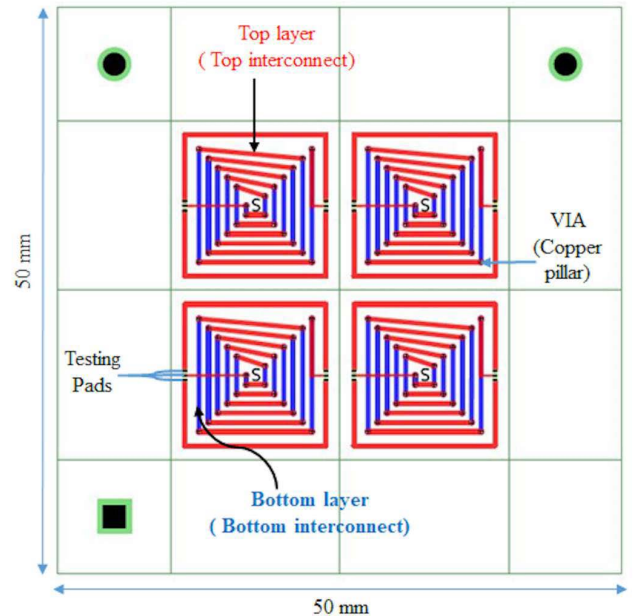


FIGURE 27. Layout of the fabricated 3-D spiral inductors on PCB.

The first three components (i.e., M_1, M_2, M_3) are contributed by pillars and the last two components (i.e., M_4, M_5) are contributed by interconnects.

APPENDIX IV. AIR-CORE 3-D SPIRAL INDUCTOR ON PCB

An air-core 3-D spiral inductor is implemented on PCB within the area of 100 mm² to validate the analytical

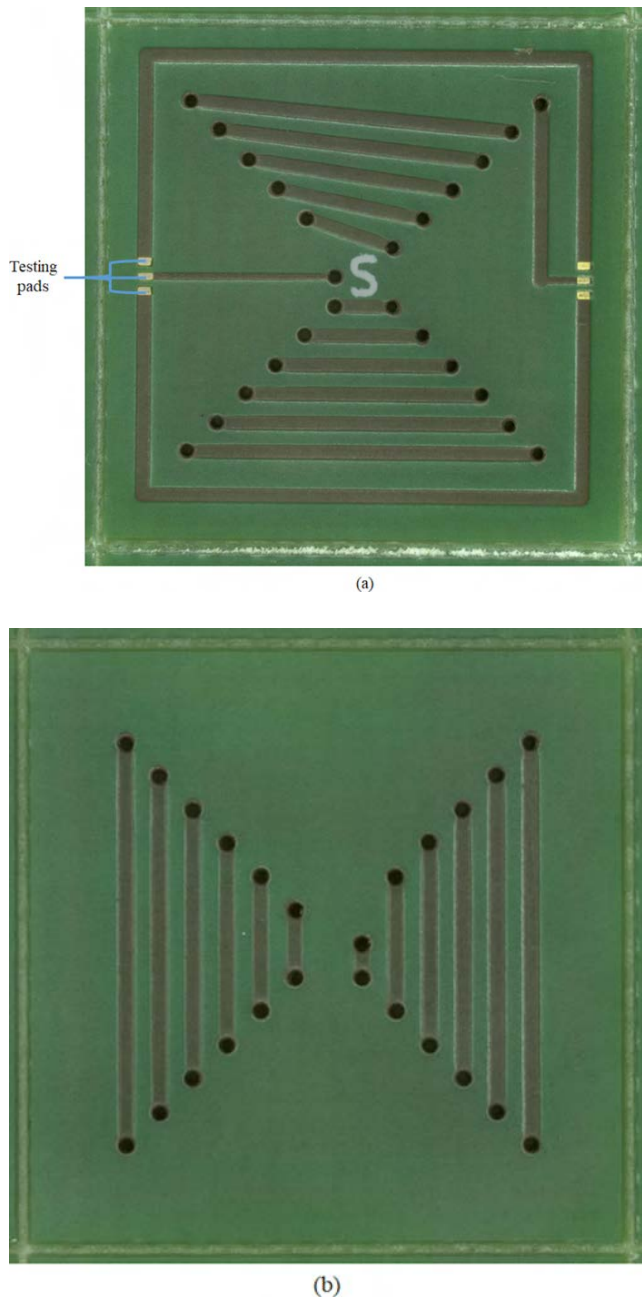


FIGURE 28. Three dimensional (3-D) spiral inductor with air-core on PCB: (a) Top view and (b) Bottom view.

expression for winding inductance. The design parameters are summarized in Table 5. Totally, four inductors are implemented on a PCB board size of $50\text{ mm} \times 50\text{ mm}$, as shown in Fig. 27. The top and bottom views of the fabricated inductor are shown in Fig. 28(a) and (b), respectively.

Next, we compare the analytical model, the FEA simulation, and the measurements in Table 6.

ACKNOWLEDGMENT

The authors would like to thank the members of the Integrated Magnetics Group for providing magnetic thin-film

measurement data (Co-Zr-Ta-B) and for facilitating electrical characterization of the PCB inductor.

REFERENCES

- [1] C. O. Mathúna, N. Wang, S. Kulkarni, and S. Roy, "Review of integrated magnetics for power supply on chip (PwrSoC)," *IEEE Trans. Power Electron.*, vol. 27, no. 11, pp. 4799–4816, Nov. 2012.
- [2] E. Candan, "Improving data center power delivery efficiency and power density with differential power processing and multilevel power converters." Ph.D. dissertation, Dept. Electrical Comput. Eng., Univ. Illinois Urbana-Champaign, Champaign, IL, USA, 2019.
- [3] X. Yu, M. Kim, F. Herrault, C. H. Ji, J. Kim, and M. G. Allen, "Silicon-embedding approaches to 3-D toroidal inductor fabrication," *J. Microelectromech. Syst.*, vol. 22, no. 3, pp. 580–588, Jun. 2013.
- [4] C. Ó Mathúna, T. O'Donnell, N. Wang, and K. Rinne, "Magnetics on silicon: An enabling technology for power supply on chip," *IEEE Trans. Power Electron.*, vol. 20, no. 3, pp. 585–592, May 2005.
- [5] H. T. Le, Y. Nour, Z. Pavlovic, C. O'Mathúna, A. Knott, F. Jensen, A. Han, S. Kulkarni, and Z. Ouyang, "High-Q three-dimensional microfabricated magnetic-core toroidal inductors for power supplies in package," *IEEE Trans. Power Electron.*, vol. 34, no. 1, pp. 74–85, Jan. 2019.
- [6] C. O. Mathuna, N. Wang, S. Kulkarni, and S. Roy, "Powder supply on chip (integration of inductors and capacitors with active semiconductors)," in *Proc. 24th Int. Symp. Power Semicond. Devices (ICs)*, Jun. 2012, pp. 319–323.
- [7] R. Foley, F. Waldron, J. Slowey, A. Alderman, B. Narveson, and S. C. O'Mathuna, "Technology roadmapping for power supply in package (PSiP) and power supply on chip (PwrSoC)," in *Proc. 25th Annu. IEEE Appl. Power Electron. Conf. Exposit. (APEC)*, Feb. 2010, pp. 525–532.
- [8] H. T. Le, "3D microfabricated air-core inductors for integrated power supply," in *Proc. IEEE Workshop Integr. Power Convers. Power Manag. (PwrSoC)*, 2018, pp. 1–35.
- [9] C. Shetty, "Studying the dynamics of the second-order DC–DC converter with single and multi-loop feedback for the optimum bandwidth," in *Proc. 4th Int. Conf. Adv. Comput. Commun.*, Aug. 2014, pp. 352–355.
- [10] N. Wang, J. Hannon, R. Foley, K. McCarthy, T. O'Donnell, K. Rodgers, F. Waldron, and C. O. Mathuna, "Integrated magnetics on silicon for power supply in package (PSiP) and power supply on chip (PwrSoC)," in *Proc. 3rd Electron. Syst. Integr. Technol. Conf. (ESTC)*, Sep. 2010, pp. 1–6.
- [11] S. Mondal, S.-B. Cho, and B. C. Kim, "Modeling and crosstalk evaluation of 3-D TSV-based inductor with ground TSV shielding," *IEEE Trans. Very Large Scale Integr. (VLSI) Syst.*, vol. 25, no. 1, pp. 308–318, Jan. 2017.
- [12] U. R. Tida, R. Yang, C. Zhuo, and Y. Shi, "On the efficacy of through-silicon-via inductors," *IEEE Trans. Very Large Scale Integr. (VLSI) Syst.*, vol. 23, no. 7, pp. 1322–1334, Jul. 2015.
- [13] C. Shetty, "A detailed study of Qdc of 3D micro air-core inductors for integrated power supplies: Power supply in package (PSiP) and power supply on chip (PSoC)," *Power Electron. Devices Compon.*, vol. 2, Jun. 2022, Art. no. 100006.
- [14] S. Kulkarni, D. Li, D. Jordan, N. Wang, and C. O. Mathúna, "PCB embedded bondwire inductors with discrete thin-film magnetic core for power supply in package," *IEEE J. Emerg. Sel. Topics Power Electron.*, vol. 6, no. 2, pp. 614–620, Jun. 2018.
- [15] X. Fang, R. Wu, L. Peng, and J. K. O. Sin, "A novel integrated power inductor with vertical laminated core for improved L/R ratios," *IEEE Electron Device Lett.*, vol. 35, no. 12, pp. 1287–1289, Dec. 2014.
- [16] F. C. Lee, J. D. V. Wyk, D. Boroyevich, G.-Q. Lu, Z. Liang, and P. Barbosa, "Technology trends toward a system-in-a-module in power electronics," *IEEE Circuits Syst. Mag.*, vol. 2, no. 4, pp. 4–22, 4th Quart., 2002.
- [17] J. Li, V. F.-G. Tseng, Z. Xiao, and H. Xie, "A high-Q in-silicon power inductor designed for wafer-level integration of compact DC–DC converters," *IEEE Trans. Power Electron.*, vol. 32, no. 5, pp. 3858–3867, May 2017.
- [18] Y. I. Bontzios, M. G. Dimopoulos, and A. A. Hatzopoulos, "Prospects of 3D inductors on through silicon vias processes for 3D ICs," in *Proc. IEEE/IFIP 19th Int. Conf. VLSI Syst.-Chip*, Oct. 2011, pp. 90–93.
- [19] H. T. Le, Y. Nour, A. Han, F. Jensen, Z. Ouyang, and A. Knott, "Micro-fabricated air-core toroidal inductor in very high-frequency power converters," *IEEE J. Emerg. Sel. Topics Power Electron.*, vol. 6, no. 2, pp. 604–613, Jun. 2018.
- [20] G. Zulauf, W. Liang, and J. Rivas-Davila, "A unified model for high-power, air-core toroidal PCB inductors," in *Proc. IEEE 18th Workshop Control Model. Power Electron. (COMPEL)*, Jul. 2017, pp. 1–8.

- [21] S. Chen, Y. Li, and R. Wu, "Inductance to DC resistance ratio optimization of on-chip closed-core spiral power inductors," in *Proc. IEEE Int. Conf. Electron Devices Solid-State Circuits (EDSSC)*, Aug. 2016, pp. 52–55.
- [22] R. Meere, T. O'Donnell, S. Kulkarni, S. Roy, and S. C. O'Mathuna, "Magnetic-core and air-core inductors on silicon: A performance comparison up to 100 MHz," *IEEE Trans. Magn.*, vol. 47, no. 10, pp. 4429–4432, Oct. 2011.
- [23] M. Araghchini, J. Hen, V. Doan-Nguyen, D. V. Harburg, D. Jin, J. Kim, M. S. Kim, S. Lim, B. Lu, D. Piedra, and J. Qiu, "A technology overview of the powerchip development program," *IEEE Trans. Power Electron.*, vol. 28, no. 9, pp. 4182–4201, Sep. 2013.
- [24] J. Kim, J.-K. Kim, M. Kim, F. Herrault, and M. G. Allen, "Microfabrication of toroidal inductors integrated with nanolaminated ferromagnetic metallic cores," *J. Micromech. Microeng.*, vol. 23, no. 11, Oct. 2013, Art. no. 114006.
- [25] D. S. Gardner, G. Schrom, P. Hazucha, F. Paillet, T. Karnik, S. Borkar, R. Hallstein, T. Dambrauskas, C. Hill, C. Linde, W. Worwag, R. Baresel, and S. Muthukumar, "Integrated on-chip inductors using magnetic material (invited)," *J. Appl. Phys.*, vol. 103, no. 7, Oct. 2008, Art. no. 07E927.
- [26] C. R. Sullivan, J. Qiu, D. V. Harburg, and C. G. Levey, "Batch fabrication of radial anisotropy toroidal inductors," in *Proc. Int. Symp. 3D Power Electron. Integr. Manuf. (PEIM)*, Jun. 2016, pp. 1–15.
- [27] T. Xu, J. Sun, H. Wu, H. Li, H. Li, and Z. Tao, "3D MEMS in-chip solenoid inductor with high inductance density for power MEMS device," *IEEE Electron Device Lett.*, vol. 40, no. 11, pp. 1816–1819, Nov. 2019.
- [28] H. Wu, S. Zhao, D. S. Gardner, and H. Yu, "Improved high frequency response and quality factor of on-chip ferromagnetic thin film inductors by laminating and patterning Co-Zr-Ta-B films," *IEEE Trans. Magn.*, vol. 49, no. 7, pp. 4176–4179, Jul. 2013.
- [29] H. K. Krishnamurthy, V. Vaidya, P. Kumar, R. Jain, S. Weng, S. T. Kim, G. E. Matthew, N. Desai, X. Liu, K. Ravichandran, and J. W. Tschanz, "A digitally controlled fully integrated voltage regulator with on-die solenoid inductor with planar magnetic core in 14-nm Tri-gate CMOS," *IEEE J. Solid-State Circuits*, vol. 53, no. 1, pp. 8–19, Jan. 2018.
- [30] N. Wang, B. B. Doris, A. B. Shehata, E. J. O'Sullivan, S. L. Brown, S. Rosnagel, J. Ott, L. Gignac, M. Massouras, L. T. Romankiw, and H. L. Deligianni, "High-Q magnetic inductors for high efficiency on-chip power conversion," in *IEDM Tech. Dig.*, Dec. 2016, pp. 35.3.1–35.3.4.
- [31] K. B. Ashby, I. A. Koullias, W. C. Finley, J. J. Bastek, and S. Moianian, "High Q inductors for wireless applications in a complementary silicon bipolar process," *IEEE J. Solid-State Circuits*, vol. 31, no. 1, pp. 4–9, Jan. 1996.
- [32] J.-B. Yoon, B.-K. Kim, C.-H. Han, E. Yoon, and C.-K. Kim, "Surface micromachined solenoid on-Si and on-glass inductors for RF applications," *IEEE Electron Device Lett.*, vol. 20, no. 9, pp. 487–489, Sep. 1999.
- [33] D. V. Harburg, A. J. Hanson, J. Qiu, B. A. Reese, J. D. Ranson, D. M. Otten, C. G. Levey, and C. R. Sullivan, "Microfabricated racetrack inductors with thin-film magnetic cores for on-chip power conversion," *IEEE J. Emerg. Sel. Topics Power Electron.*, vol. 6, no. 3, pp. 1280–1294, Sep. 2018.
- [34] H. T. Le, R. I. Haque, Z. Ouyang, S. W. Lee, S. I. Fried, D. Zhao, M. Qiu, and A. Han, "MEMS inductor fabrication and emerging applications in power electronics and neurotechnologies," *Microsyst. Nanoeng.*, vol. 7, no. 1, pp. 1–22, Aug. 2021.
- [35] C. D. Meyer, S. S. Bedair, B. C. Morgan, and D. P. Arnold, "A micromachined wiring board with integrated microinductor for chip-scale power conversion," *IEEE Trans. Power Electron.*, vol. 29, no. 11, pp. 6052–6063, Nov. 2014.
- [36] M. Bathily, B. Allard, and F. Hasbani, "A 200-MHz integrated buck converter with resonant gate drivers for an RF power amplifier," *IEEE Trans. Power Electron.*, vol. 27, no. 2, pp. 610–613, Feb. 2012.
- [37] P. Shamsi and B. Fahimi, "Design and development of very high frequency resonant DC–DC boost converters," *IEEE Trans. Power Electron.*, vol. 27, no. 8, pp. 3725–3733, Aug. 2012.
- [38] R. Wu and J. K. O. Sin, "A novel silicon-embedded coreless inductor for high-frequency power management applications," *IEEE Electron Device Lett.*, vol. 32, no. 1, pp. 60–62, Jan. 2011.
- [39] D. Hart, *Power Electronics*. New York, NY, USA: McGraw-Hill, 2011, pp. 198–211.
- [40] Texas Instruments. (Apr. 2021). *Time-Saving and Cost-Effective Innovations for EMI Reduction in Power Supplies*. SLYY200. [Online]. Available: <https://www.ti.com/lit/wp/slyy200/slyy200.pdf>
- [41] H. J. Zhang and S. Young. (2020). *Speed Up the Design of EMI Filters for Switch-Mode Power Supplies*. [Online]. Available: <https://www.analog.com/media/en/analog-dialogue/volume-54/number-2/speed-up-the-design-of-emi-filters-for-switch-mode-power-supplies.pdf>
- [42] Analog Devices. (2014). *Recommendations for Control of Radiated Emissions With Isopower Devices*. AN-0971. [Online]. Available: <https://www.analog.com/media/en/technical-documentation/app-notes/an-0971.pdf>
- [43] CUI INC. (2019). *Electromagnetic Compatibility Considerations for Switching Power Supplies*. [Online]. Available: <https://www.cui.com/catalog/resource/download/emi-considerations-for-switching-power-supplies.pdf>
- [44] K. Kam, D. Pommerenke, F. Centola, C.-W. Lam, and R. Steinfeld, "EMC guideline for synchronous buck converter design," in *Proc. IEEE Int. Symp. Electromagn. Compat.*, Aug. 2009, pp. 47–52.
- [45] E. B. Rosa, "The self and mutual inductances of linear conductors," *Bull. Bur. Standards*, vol. 4, no. 2, pp. 301–344, Sep. 1907.
- [46] R. De Smedt, "Addition to 'DC internal inductance for a conductor of rectangular cross Sectio,'" *IEEE Trans. Electromagn. Compat.*, vol. 51, no. 3, pp. 875–876, Aug. 2009.
- [47] H. T. Le, I. Mizushima, Y. Nur, P. T. Tang, A. Knott, Z. Ouyang, F. Jensen, and A. Han, "Fabrication of 3D air-core MEMS inductors for very-high-frequency power conversions," *Microsyst. Nanoeng.*, vol. 4, no. 1, pp. 1–9, Jan. 2018.
- [48] C. R. Paul, *Inductance: Loop and Partial*. New York, NY, USA: Wiley, 2010, pp. 274–285.
- [49] H. M. Greenhouse, "Design of planar rectangular microelectronic inductors," *IEEE Trans., Hybrids, Packag.*, vol. HP-10, no. 2, pp. 101–109, Jun. 1974.
- [50] R. Anthony, E. Laforge, D. P. Casey, J. F. Rohan, and C. O'Mathuna, "High-aspect-ratio photoresist processing for fabrication of high resolution and thick micro-windings," *J. Micromech. Microeng.*, vol. 26, no. 10, 2016, Art. no. 105012.
- [51] D. C. Smallwood, P. McCloskey, C. O'Mathuna, D. P. Casey, and J. F. Rohan, "Methods for latent image simulations in photolithography with a polychromatic light attenuation equation for fabricating VIAs in 2.5D and 3D advanced packaging architectures," *Microsyst. Nanoeng.*, vol. 7, no. 1, May 2021.
- [52] Z. Xu and J.-Q. Lu, "High-speed design and broadband modeling of through-strata-vias (TSVs) in 3D integration," *IEEE Trans. Compon., Packag., Manuf. Technol.*, vol. 1, no. 2, pp. 154–162, Feb. 2011.
- [53] K. Salah, Y. Ismail, and A. El-Rouby, *Arbitrary Modeling of TSVs for 3D Integrated Circuits*. Cham, Switzerland: Springer, 2014, pp. 149–151.
- [54] C. Shetty, Y. Kandeel, L. Ye, S. O'Driscoll, P. McCloskey, M. Duffy, and C. O. Mathuna, "Analytical expressions for inductances of 3-D air-core inductors for integrated power supply," *IEEE J. Emerg. Sel. Topics Power Electron.*, vol. 10, no. 2, pp. 1363–1383, Apr. 2022.
- [55] C. R. Paul, *Inductance: Loop and Partial*. New York, NY, USA: Wiley, 2010, pp. 209–224.
- [56] J. Kim, J. S. Pak, J. Cho, E. Song, J. Cho, H. Kim, T. Song, J. Lee, H. Lee, K. Park, S. Yang, M. S. Suh, K. Y. Byun, and J. Kim, "High-frequency scalable electrical model and analysis of a through silicon via (TSV)," *IEEE Trans. Compon., Packag., Manuf. Technol.*, vol. 1, no. 2, pp. 181–195, Feb. 2011.
- [57] R. Anthony, C. Ó. Mathúna, and J. F. Rohan, "Palladium activated self-assembled monolayer for magnetics on silicon applications," *Phys. Proc.*, vol. 75, pp. 1207–1213, Jan. 2015.
- [58] C.-K. Kim, Y.-H. Yoon, D. Kwon, S. Kim, G.-W. Yoon, M. W. Rhee, J. Yun, I. Park, and J.-B. Yoon, "First lateral contact probing of 55 μm fine pitch micro-bumps," *J. Microelectromech. Syst.*, vol. 27, no. 6, pp. 1114–1123, Sep. 2018.
- [59] C. H. Ahn and M. G. Allen, "A comparison of two micromachined inductors (bar- and meander-type) for fully integrated boost DC/DC power converters," *IEEE Trans. Power Electron.*, vol. 11, no. 2, pp. 239–245, Mar. 1996.
- [60] B. Orlando, R. Hida, R. Cuchet, M. Audoin, B. Viala, D. Pellissier-Tanon, X. Gagnard, and P. Ancy, "Low-resistance integrated toroidal inductor for power management," *IEEE Trans. Magn.*, vol. 42, no. 10, pp. 3374–3376, Oct. 2006.
- [61] R. Meere, T. O'Donnell, H. J. Bergveld, N. Wang, and S. C. O'Mathuna, "Analysis of microinductor performance in a 20–100 MHz DC/DC converter," *IEEE Trans. Power Electron.*, vol. 24, no. 9, pp. 2212–2218, Sep. 2009.

- [62] X. Fang, R. Wu, L. Peng, and J. K. O. Sin, "A novel silicon-embedded toroidal power inductor with magnetic core," *IEEE Electron Device Lett.*, vol. 34, no. 2, pp. 292–294, Feb. 2013.
- [63] M. Wang, J. Li, K. D. T. Ngo, and H. Xie, "A surface-mountable microfabricated power inductor in silicon for ultracompact power supplies," *IEEE Trans. Power Electron.*, vol. 26, no. 5, pp. 1310–1315, May 2011.
- [64] R. Anthony, N. Wang, D. P. Casey, Ó. Mathúna, and J. F. Rohan, "MEMS based fabrication of high-frequency integrated inductors on Ni–Cu–Zn ferrite substrates," *J. Magn. Magn. Mater.*, vol. 406, pp. 89–94, May 2016.
- [65] J. Li, K. D. T. Ngo, G.-Q. Lu, and H. Xie, "Wafer-level fabrication of high-power-density MEMS passives based on silicon molding technique," in *Proc. 7th Int. Conf. Integr. Power Electron. Syst. (CIPS)*, Mar. 2012, pp. 1–5.
- [66] F. W. Grover, *Inductance Calculations*. New York, NY, USA: Dover, 1973, pp. 45–47.



(UCC), Cork, Ireland.

His research interests include novel circuit topologies, design of digital control systems, wide bandgap semiconductors, such as SiC and gallium nitride (GaN), the design of magnetic components, which include inductors, coupled-inductors and transformers, for switched mode power converters, design and modeling of 3D inductors for power supply-in-package (PSiP), and power supply-on-chip (PwrSoC) applications.



DANIEL C. SMALLWOOD received the B.S. degree (*magna cum laude*) in chemical engineering from The University of Alabama in Huntsville, in 2015, and the Ph.D. degree in engineering science (physics, optics and magnetics) from the Tyndall National Institute University College Cork, Ireland, in 2021. During his Ph.D., he worked on the project ADEPT: Advanced Integrated Power Magnetism Technology—From Atoms to Systems. His research focused on the development of next generation integrated magnetic devices with increased efficiency and miniaturization. His research also focused on light-matter interactions within the context of micro/nano engineering. He taught the undergraduate and postgraduate level in the fields of chemistry, engineering and micro/nano systems at UCC/Tyndall. He has worked in several industry and research settings ranging from renewable energy to biotechnology and power electronics. His current research interests include hybrid quantum systems, opto/electromechanics, magnetism, optics, energy, electrochemistry, materials, micro/nano systems, and computational science.

• • •